Dynamics of a Three-Wheel Vehicle with Tadpole Design

by

Azadeh Zandieh

A thesis
presented to the University of Waterloo
in fulfillment of the
thesis requirement for the degree of
Master of Science
in
Mechanical Engineering

Waterloo, Ontario, Canada, 2014

AUTHOR'S DECLARATION

I hereby declare that I am the sole author of this thesis. This is a true copy of the thesis, including any required final revisions, as accepted by my examiners.

I understand that my thesis may be made electronically available to the public.

Azadeh Zandieh

Abstract

This study investigates the effect of applying camber angle on the handling, lateral stability, and ride comfort of a three-wheeled vehicle, which has two wheels in the front and one in the back, known as a tadpole design. Since the three-wheeled vehicle in this study is a light and narrow vehicle, controlling the stability of this vehicle, particularly during turning, cornering, and harsh maneuver is a very challenging task. To enhance the stability of this three-wheeled vehicle, an active camber system has been added to the vehicle suspension system. Effects of applying active camber angles on corresponding stability parameter, rollover acceleration threshold and skidding acceleration threshold, in different conditions are accordingly calculated (by simulating the movement of the vehicle in MATLAB/Simulink). Next, the handling of the vehicle was analyzed by studying the effect of camber angle in different vehicle speed on the yaw rate via deriving the corresponding transfer functions and plotting the bode diagrams. Furthermore, the ride comfort of the vehicle is analyzed and forces generated on each part of the suspension system are determined by modelling the vehicle movement using Multibody Dynamics Adams software.

Acknowledgements

First and foremost, I would like to thank my supervisor, Professor Amir Khajepour, for all his guidance and support throughout my master's research. To put all my appreciation in a sentence, I should say I was honored to do my master's project under his supervision.

I would also like to pass my great appreciation to Professor Avesta Goodarzi and Dr. Alireza Kasaiezadeh and Dr. Alireza Pazooki for their insightful guidance and support throughout my master's degree studies. Many thanks go to my friends and colleagues at the University of Waterloo for their patience and support.

I would also like to thank my friends and colleagues. In particular, I would like to extend my gratitude to Hadi Izadi for his remarkable help towards finishing this thesis.

Last but not least, my sincere gratitude goes to my father, Mehdi, and my sister, Ghazaleh, for all their support and patience, not only during my master's degree studies, but also throughout my whole life.

Dedication

I would like to dedicate this thesis to my mother who has always been the inspiration of my life.

Table of Contents

List of Figures

List of Tables

Chapter 1. Introduction

Growing population in cities and rising number of vehicles have brought car designer into a new challenge for production of small and fuel efficient, but safe vehicles. In this vein, a new generation of small cars have recently come into existence. Nowadays, because of their low fuel consumption and ease of driving and parking in populated cities, they are gaining more attention. For instance, some three wheelers have already being used as part of the public transportation system in several countries such as India, Thailand, Peru, China, and even Italy. Electric three wheelers have the advantage of lower fuel costs and zero emissions.

Despite their popularity, three-wheelers, due to their typical light and narrow design, have one major drawback: They are not very stable in harsh maneuvers. Different methods have been proposed to improve their stability. Among all, applying camber angle to the wheels and tilting the body are the most promising approaches. Choosing between them, however, completely depends on the purpose of the vehicle. That is, for manoeuvring and fast driving, usually tilting system is preferable, while for normal commuting in cities, cambering system is recommended.

In this thesis, an electric three-wheeled vehicle, which has a tadpole design (i.e., has two wheels in the front and one in the back), will be introduced. Given that this vehicle is designed for daily application in urban environments, with top speed of 80 km/h, cambering system will be incorporated in each wheel in order to improve the handling and stability of this vehicle. It should be also noted that for this electric vehicle, an in-wheel suspension system has been chosen. This has been done due to the fact that the three-wheeled vehicle of our study is small, while having a narrow in-wheel suspension system allows providing more space for passengers and cargo.

In the first step and in order to study the effect of applying camber angle on handling and in particular, on the yaw rate, at various speeds, transfer functions for outputs of yaw rate to inputs of camber angle and momentum will be derived and the corresponding bode diagrams will be plotted.

In the next step, the effects of applying camber angles on the rollover acceleration threshold and accordingly, on its lateral stability, will be studied. For this purpose, three different approaches will be considered. The first approach is based on applying one negative and one positive camber angle to the front wheels. In particular, the inside-turn wheel will have a positive camber angle while the other one will have a negative camber angle. Applying two negative camber angles to both front wheels will also be investigated. Finally, the impact of non-symmetric camber angles on all wheels will be studied. In all the above-mentioned approaches, the lateral stability of the vehicle via calculating the corresponding lateral acceleration thresholds will be calculated for comparison. At last, skidding thresholds (as another factor determining the lateral instability of a vehicle) for various types of roads will be calculated and, by comparing the skidding analysis results with those obtained from rollover threshold analysis, the occurrence of skidding in relation to rollover will be illustrated.

After studying the handling and lateral stability of the three-wheeled vehicle, the ride quality of the vehicle will be studied. To do so, the ratio of the vibration amplitudes of the sprung mass to the magnitude of the surface profile irregularities will be determined. Furthermore, the influence of the unsprung mass on the vehicle comfort will be studied. In addition, ride comfort analysis will be carried out on two different types of roads, a single haversine bump and a sinusoidal road. Ride comfort parameters, including vertical displacement, vertical acceleration, and pitch angle of the sprung mass will be calculated and the ride comfort of the vehicle will be discussed accordingly.

In order to optimize and verify the design of the in-wheel suspension system for this three-wheeled vehicle, in the last part, the imposed forces to the key points of the suspension system will be analyzed for each corner module. To do so, in the first methodology, 1g lateral, 2g vertical, and 3g longitudinal acceleration will be applied to the stationary vehicle. In this mode, all forces at all joints of the suspension system will be calculated by using Multibody Dynamics Adams software. The dynamics of the vehicle on different types of roads will be simulated and subsequently, all forces at all joints of the suspension system will be estimated on different roads. In the end, the comparisons between these two methods (i.e., static and dynamic analysis) will be performed in order to determine if the maximum forces on the moving wheels are exceeding those obtained in the reference static analysis. Also vertical forces on wheels will be calculated, which basically will make possible determining the proper tire type for the three-wheeled vehicle of our study.

Chapter 2. Literature Review, Background, and Problem Definition

In this chapter, vehicle handling and stability as well as the parameters affecting them will be introduced first. Next, details of various systems employed to improve the handling and lateral stability will be discussed. Then, vehicle ride comfort, which is directly affected by the properties of the vehicle suspension system, will be discussed. In the end, introduction of a cambering system to the suspension system of the three-wheeled vehicle will be illustrated.

2.1 Handling

Handling quality is basically the way that a vehicle responds to a driver's commands, considering the environment that the vehicle is surrounded by, such as wind and road conditions, which affect the body and tires, respectively [1]. In general, if the vehicle and steer wheels are easy to control, it is called that the vehicle has a good handling [2]. Because of the importance of handling quality, many articles are published every year on analyzing and improving the handling quality of different cars. Sometimes, the concept of handling is confused with comfortable cornering and turning. Turning and cornering are actually about lateral acceleration, while handling is the vehicle quality in providing feedback to the driver for a better and easier control [3]. In general, handling quality can be considered in three categories of resistance to rollover, steady state behaviour, and transient behaviour [4].

In general and in order to provide a good handling when a vehicle is turning, accelerating, braking, and also during harsh maneuvers, pitch and roll acceleration should be minimized [5]. Besides, to have a good handling, it is also essential to have a stiff chassis and suspension system [6]. The parameter, which can be defined to determine the influence of these factors on the handling of a particular vehicle, is the under-steer coefficient (K_{us}). This factor for a two-wheeled vehicle (bicycle model) can be found from [1]

$$K_{us} = \frac{W_f}{C_{\alpha f}} - \frac{W_r}{C_{\alpha r}} \qquad \textbf{(2-1)}$$

where W_f and W_r are the normal forces acting on the front and rear tires, respectively, while cornering stiffness of each of the front and rear tires are $C_{\alpha f}$ and $C_{\alpha r}$. The magnitude of the under-steer coefficient basically determines the behaviour of the vehicle during a turn. In particular, for a constant

steer angle and at increasing longitudinal speed, a vehicle which tends to deviate to the outside of turn is called an under-steered vehicle. In the under-steer regime, the magnitude of the under-steer coefficient is basically larger than zero (i.e., K_{us}>0). At the same steer angle and longitudinal speed, an over-steered vehicle (i.e., K_{us}<0), on the other hand, tends to go to the inside of the turn, while a neutral steered vehicle (i.e., K_{us}=0) will stays completely on the turn path (see Figure 2-1).

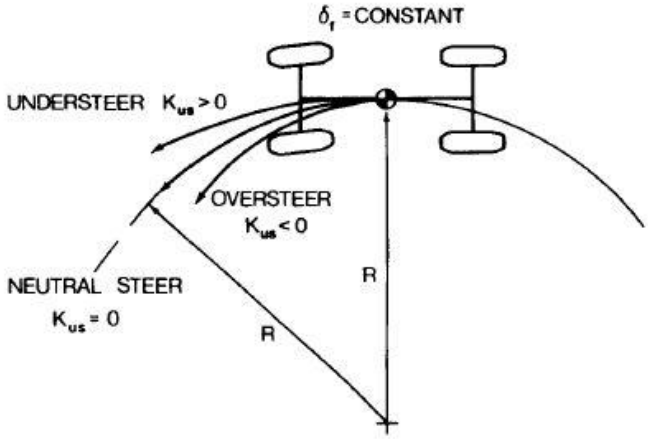

Figure 2-1. Curvature response of neutral steered, under-steered, and over-steered vehicles at a fixed steer angle [1].

In principle, when K_{us} is zero, side slip angles of front and rear wheels are equal ($\alpha_f=\alpha_r$, $W_f/C_{\alpha f} = W_r/C_{\alpha r}$, and $\delta_f= L/R$) (here, L is the length of vehicle and R is the radius of the turn) [1,7]. In the under-steer regime, when $K_{us}>0$, however, slip angle of the front wheel is larger than that of the rear one (i.e., $\alpha_f>\alpha_r$, $W_f/C_{\alpha f} > W_r/C_{\alpha}$, and $\delta_f> L/R$). This basically implies that when the vehicle is accelerating with a constant steer angle, the turning radius increases. In the over-steer region, however, when the vehicle is accelerating with a constant steer angle, the turning radius tends to get smaller (i.e., $\alpha_f<\alpha_r$, $W_f/C_{\alpha f} < W_r/C_{\alpha}$, and $\delta_f< L/R$). In general, to have a good handling, under-steer coefficient in the range of 2 to 6 deg/g is preferable. It should be noted that under-steer coefficient is different for different types of vehicles (such as for sedans, sports cars, trucks, etc.) (see Figure 2-2) [1,8].

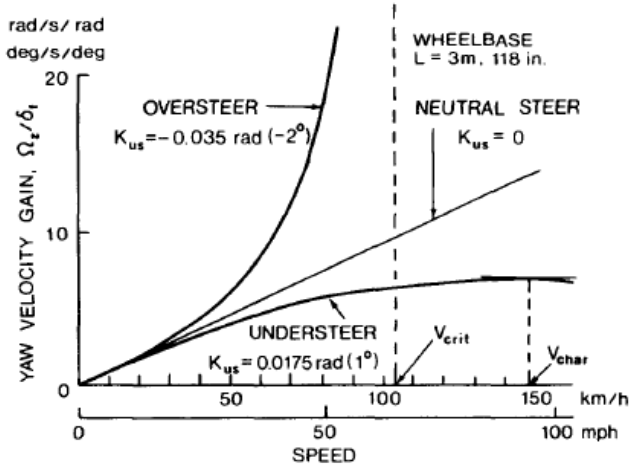

Figure 2-2. Steer angle vs. speed of neutral steer, under-steer, and over-steer [1].

Other than yaw rate, the other important parameter which specifies the handling quality of a vehicle is the side slip angle. In fact, due to steer and side slip during turning, a slip angle (i.e., an angle between the moving direction of the vehicle and the heading direction) is produced. In the following subsection, yaw rate and side slip angle as well as the different methods employed to control them in various vehicles will be discussed in detail.

2.1.1 Yaw rate, side slip angle, and vehicle path

In this part, yaw rate and side slip angle, as two important parameters affecting the handling of a vehicle, are introduced. To do so, first we need to define the Society of Automotive Engineers (SAE) coordinate system, based on which all equations and calculations in this thesis have been derived (see Figure 2-3) [3]. In the SAE coordinate system, the *x* axis is the axis located along the longitudinal axis of the vehicle in the positive direction when the vehicle is moving forward, while *y* and *z* axes are considered right-handed to the *x* axis.

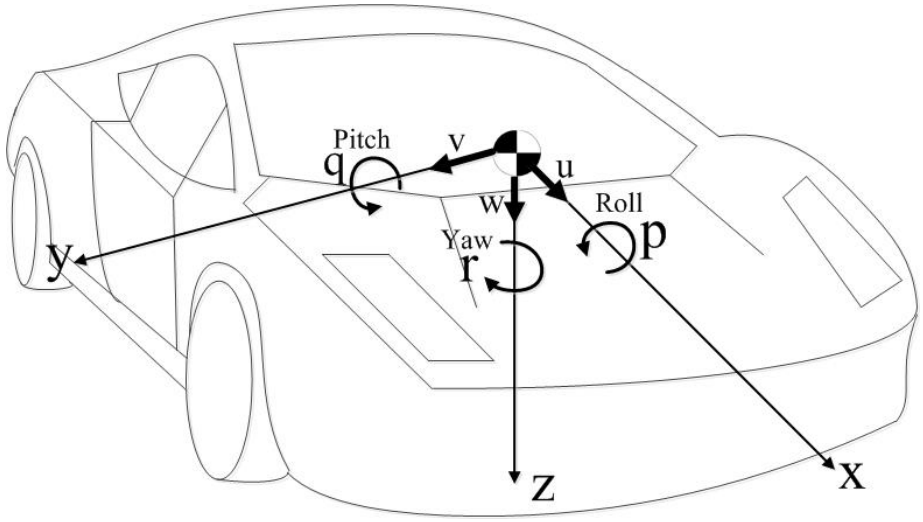

Figure 2-3. SAE vehicle coordinate orientations, where the zero point of the coordinate system is attached to the vehicle centre of gravity (CG).

In Figure 2-3, yaw is defined by the parameter *r*, the rotation produced about the *z* axis. In here, pitch (*q*) is the rotation about the *y* axis, while roll (*p*) is the rotation about the *x* axis. Lateral speed, longitudinal speed, and vertical speed are defined as *v*, *u* and *w*, respectively. To have a better turn, one needs to control and optimize the lateral velocity, and accordingly, the yaw rate. The other important parameter, which has to be controlled in order to improve the handling of a vehicle, is side slip angle. Side slip angle α is the angle between the direction of wheel heading and the direction of wheel travel, as shown in Figure 2-4.

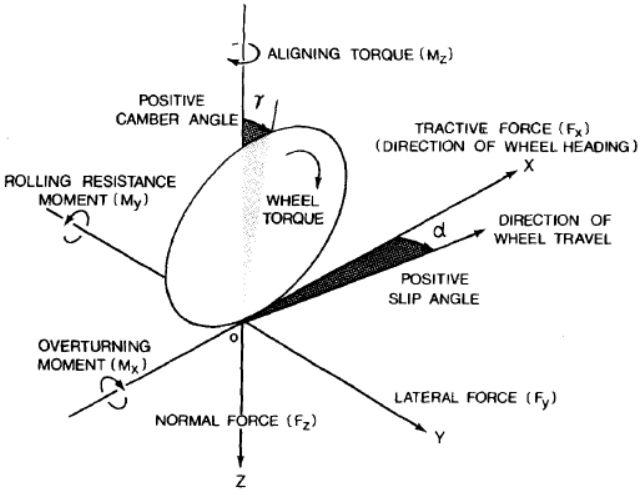

Figure 2-4. Tire axis system and side slip angle [1].

Side slip angle basically determines the lateral stability of a vehicle, which can be controlled by various methods, such as controlling the steering system and improving lateral forces on tires [9-12]. The effect of side slip angle on lateral forces, when there is no camber angle, can be quantified by a parameter called the cornering force, $F_{y\alpha} = C_\alpha \alpha$, where C_α is the cornering coefficient [1]. In general, side slip angle and the lateral forces which are produced in tires are very influential on the vehicle handling. In terms of handling, as the concept of interest in this section, side slip angles between 0 and 4 deg (called side slip magic numbers) are usually favoured [7].

Due to the fact that yaw rate and side slip angles have great influence on lateral forces and as a result, they directly affect the handling and stability of a vehicle [13], many controllers have been developed in order to keep these values as much desirable as possible [14-18]. For instance, Matsumoto and Tomizuka [19] developed a controller to control the yaw rate and lateral speed of a four-wheeled vehicle independently. In their research, the differential torque between the front wheels, differential torque between the rear wheels, and also the steer angle for the rear wheels were used as inputs to the controller [19]. An experimental study was also carried out to verify the performance of the controller [19]. In another study, Zeyada et al. [20] proposed a control method by using active steering and differential braking control by using fuzzy-logic interference system to control and minimize the yaw rate. This combination method basically introduced a controller that did not have disadvantages of either differential braking or active steering during high lateral acceleration and harsh maneuver [20]. A torque-vectoring controller to control the yaw rate was also established by Sabbioni et al. [21] for an electric vehicle. Using this system, it was shown that the peak values of oscillation for side slip angle and yaw rate can be decreased [21]. Sakhalkar et al. [22] also showed that by adding a torque vectoring control system to change the yaw rate of a four-wheeled vehicle, the vehicle could be kept on a desired path. In their system, when the yaw rate was not desired, by changing the steer wheel input, different torques were applied to the left and right wheels in order to keep the vehicle on a desired path [22]. A nonlinear path tracking controller was also developed by Zakaria et al. [23]. Their system was based on a steering wheel and lateral control system. The control algorithm that was developed by this group could calculate the vehicle lateral acceleration error by using yaw rate and steer wheel sensors, in order to obtain feedback data [23]. In another study, a proportional-integral-derivative (PID) steer controller, which could regulate the yaw rate by using Constant Radius Constant Speed (CRCS), was developed by Liang [24]. The other way to dynamically control the

handling of a vehicle is controlling the side slip angle. Baffet et al. [25], for instance, have worked on different observers (such as The Extended Kalman Filter) to calculate the lateral speed and accordingly, the side slip angle. A Direct Yaw Moment Control (DYMC) is also another very effective tool to control yaw rate and side slip angle [26].

2.1.2 Camber and tilt

In general, the most two common ways to improve the performance and stability of a three-wheeled vehicle during turning and harsh maneuver is applying camber angle to the wheels or tilt the body. In the case of wheel cambering, according to Figure 2-5, which shows car wheels from the front, camber angle is applied by tilting a wheel inward or outward. In principle, when the vertical axis of the wheel is parallel to the vertical axis of the body, there is no cambering. When the wheel goes outward or inward (relative to the body), positive or negative camber angles are applied to the wheels, respectively.

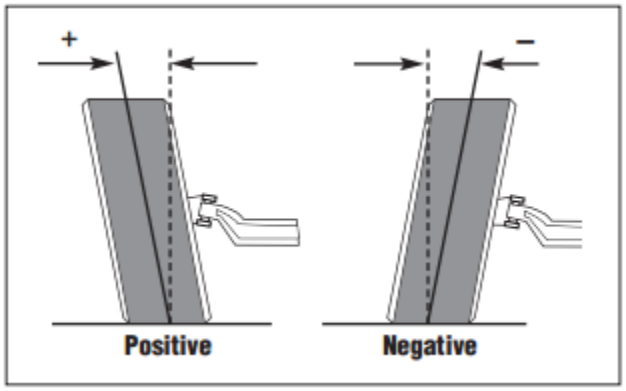

Figure 2-5. Schematic demonstration of negative and positive camber angle [27].

The advantage of applying camber angle is that by applying even a small angle, cornering becomes significantly shorter [28]. However, it should be noted that in order to improve cornering, not only applying camber angle is important, but also camber angle should be constantly and accurately controlled [29]. For instance, during turning and maneuver, if a passive camber angle is imposed to a wheel, it will change the under-steer characteristics of the vehicle. To avoid this, one essentially needs to constantly and accurately control the camber angle by using a proper controller [30].

Camber controllers can be designed in various ways. For instance, some camber controllers are working based on a proportional relationship with steer angle. Yoshino and Nozaki [31] reported on applying positive-negative camber angle, where, according to wheel steering of the front wheels, the inner-turn wheel was cambered in the negative direction while the outer-turn wheel was cambered in the positive direction. Another approach in design of a camber control can be based on having camber control in a way that wheels are always kept parallel to each other (during lateral acceleration, vertical displacement, and even roll). Cuttino et al. [32], for example, used this type of camber controller in their experiments and they verified the improvement in the lateral stability of their vehicle by simulation of the cornering of the vehicle in Multibody Dynamics Adams software.

Another approach to control the manoeuvrability and stability of a vehicle, particularly during turning and cornering, is applying a tilt angle to the body. In a vehicle with an active tilting system, the whole body bends toward the centre of turning radius in order to change the CG position, exactly similar to what motorcycle riders do during rapid turnings. Tilting systems are usually applied to narrow three-wheeled vehicles, because of their natural instability caused by their small track and the possibility of their rollover (which is more elaborate for this kind of vehicles in comparison to conventional four-wheeled vehicles) [33].

Tilting system has been traditionally applied to narrow three-wheeled vehicles in order to improve their manoeuvrability, particularly at high speeds and during large steering angles [34]. A three-wheeled vehicle, which has two passenger sits behind each other, has less space in the frontal area, and therefore, the vehicle acts like a motorcycle on roads. In a study on this type of vehicles, Berote et al. [35] has mentioned that one of the main problems associated with their vehicle was its weak rollover stability. In order to solve this problem, a hydraulic tilt mechanism was introduced to the vehicle suspension system [35]. A positive inclined tilt axis for optimizing roll incident was analyzed, where a larger yaw rate was applied at the rear wheels in comparison to that applied on the one in the front. Doing so, it was observed that the rear wheels steered into the turn, which in turn helped the turning [35]. The other important factor that Berote et al. considered was the speed of the actuator when tilt angle was applied to the body [35]. They found out that when tilt angle was applied to the body, the response time had to be slowed down in order to avoid large torques to the body [35]. Edelmam and Plochi [36], in another study, proposed a tilting system for a three wheeler, having one wheel in the front and two wheels in the back. In their study, they used a steering torque input to

change the angle of tilting in order to make the process more energy efficient. The controller they used was able to change the tilting angle according to the steering angle, which led to decrease in the possibility of the occurrence of rollover [36].

It is worthwhile mentioning that applying tilt angle to the body can be pleasant for the passengers. For instance, Will et al. [37] has mentioned in their study on a narrow Carver car (a three wheeler having two wheels in the back and one in the front) that "it is so much fun to drive when it tilts that one is even inclined to continuously zigzag along the road, which can be risky and also make it tip over".

Overall, to avoid instability of narrow vehicles, it is necessary to have either tilting system or cambering system. Choosing between cambering and tilting system for a narrow vehicle totally depends on the purpose of the vehicle. In general, for manoeuvring and fast driving, tilting system is suggested, while for daily commuting in cities, cambering system is more favourable.

2.2 Lateral stability

Lateral stability (i.e., stability of a moving vehicle about the axis perpendicular to its direction of motion) refers to the tendency of the moving vehicle to go back to its original direction when disturbed from that direction (e.g., during turning, manoeuvring, etc.). In general, the main parameters which can influence the lateral stability of a vehicle are type of tires, magnitude of the normal load, road/tire coefficient of friction, side slip angle, and lateral vibration [38].

Erdogan et al. [39] reported on development of a new lateral stability control system, in which accelerometer sensors were placed in tires in order to estimate the normal force of the tires and the road/tire friction coefficient, so it can accurately calculate the longitudinal tire forces. Based on simulation results, they showed that the system could effectively control the lateral stability of their vehicle [39]. An active front steering (AFS) controller was also proposed in order to improve a vehicle handling and lateral stability, particularly during overtaking [40]. According to the readings of the controller, additional steering angle was applied to the front wheels, resulting in better vehicle control [40]. Another parameter which has to be considered when one tries to control the lateral instability of a vehicle is vertical vibrations. Vertical vibrations can affect side slip angle, yaw velocity, lateral acceleration, lateral deviation, and accordingly, lateral stability [41].

Regardless of what causes lateral instability and how it can be controlled, lateral instability can have two catastrophic consequences: rollover and skidding, which will be discussed in the following subsections.

2.2.1 Rollover

From the time of the production of the first car, automobile factories have been trying to improve their vehicles in order to manufacture more comfortable and safer vehicles. Undoubtedly, one of the most important specifications of a safe and comfortable car is its low tendency to roll during turning, cornering, and harsh maneuver. Vehicle rollover, in general, happens when the driver lose the control of the vehicle. Because of the severe consequences which rollover might have (e.g., injuries and even deaths), it has drawn lots of attentions [42,43]. In American highways, the second most dangerous car accidents are caused because of rollover. In 2000 only, 9882 people got killed because of this undesirable tendency of light cars [44]. Generally, there are two types of rollover: tripped rollover and un-tripped rollover. Tripped rollover usually happens when the vehicle goes into skidding. During skidding, the vehicle hits an object and at that time, the vehicle starts to roll. In the case of un-tripped rollover, on the other hand, it is the driver who is the responsible for this phenomenon, particularly when he/she applies excessive steer angles to the vehicle (usually at high speeds or in panic situations) [45]. Different methods have been provided to avoid this dangerous tendency. In this connection, it is crucial to know about all constraints on the system in order not to over step those limits.

To improve the lateral stability of a vehicle and in order to hinder its rollover, it is essential to study the vehicle specifications in order to obtain the optimum rollover threshold in a particular broad range (which cannot be easily achieved), allowing the car over-turn to happen as hard as possible. Lateral acceleration threshold (also called the static stability factor (SSF)) is essentially depending on the geometry of the vehicle [5]. For instance, rollover acceleration threshold (a_y) for a four-wheeled vehicle can be determined from [5]

$$a_y = \frac{Tg}{2H} \quad \textbf{(2-2)}$$

where H is the distance of the CG from ground and T is the track width. As can be seen, in a particular road, what dictate the occurrence of rollover are the geometrical properties of the vehicle.

2.2.2 Skid

Another catastrophic consequence that lateral instability might have is skidding. Skidding usually happens on slippery roads or as a result of stopping or turning quickly. As mentioned, this dangerous phenomenon sometimes can also lead to rollover of the vehicle by hitting an obstacle during skidding. Studying skidding is not only very important for engineers who are trying to design safer cars, but also it is very crucial for accident reconstruction specialists who are trying to design safer roads [46].

In analysis of the skidding of a vehicle on a dry road, different parameters (such as vehicle weight, type of tires, longitudinal speed, etc.) should be taken into account [47]. Among all these, type of tires and accordingly, road/tire coefficient of friction, is one of the most important factors which can influence the phenomenon of skidding. As a matter of fact, in order to prevent skidding, the lateral acceleration must be bounded by the road/tire friction coefficient (μ) as described in Equation (2-3), stating [5]

$$a_{y-CG} \leq \mu g \quad \textbf{(2-3)}$$

From this perspective, it is completely clear that, for a particular vehicle on a particular road, in order to prevent (or at least delay) skidding, the value of road/tire coefficient of friction should be always kept high. In winter, for instance, when the road/tire coefficient of friction is naturally low, this can be achieved by using winter tires, snow chain, and/or emergency anti-skidding devices. In case of winter tires, it has been shown that they can significantly prevent skidding on snowy roads, although they are not very beneficial for driving on polished ice, particularly when the temperature is between -10 and 3 ^{o}C. In case of snow chain and emergency anti-skidding devices (which are basically textile covers), on the other hand, satisfactory results have been reported on preventing skidding upon driving on even icy roads [48]. There are also some controller systems (such as anti-lock brake systems (ABS)) which are able to hinder the occurrence of skidding – via controlling the longitudinal dynamics [49,50].

2.3 Ride

Ride comfort refers to satisfaction of the driver and passengers during a ride in a car. In general, ride comfort of a vehicle is directly related to the performance of the suspension system (dampers, springs, links, etc.) and chassis of the vehicle [51]. A basic two degree-of-freedom (2-DOF) quarter car model for analyzing the ride comfort for the sprung mass (m_s) (see Figure 2-6) can be defined as [1]

$$m_s \ddot{x}_s + c_u (\dot{x}_s - \dot{x}_u) + k_u (x_s - x_u) = 0 \quad \textbf{(2-4)}$$

while that for the unsprung mass (m_u) would be

$$m_u \ddot{x}_u + c_u (\dot{x}_s - \dot{x}_u) + k_u (x_s - x_u) + k_t (x_u - y) = 0 \quad \textbf{(2-5)}$$

where x_s is the vertical displacement of the sprung mass, x_u is the vertical displacement of the unsprung mass, c_u is the damping coefficient of the suspension system, k_u is the equivalent spring stiffness of the suspension, k_t is the equivalent stiffness of the tire, and y is the road input. m_s for each corner module should be calculated based the share of the static weight of the vehicle for that particular corner module [1].

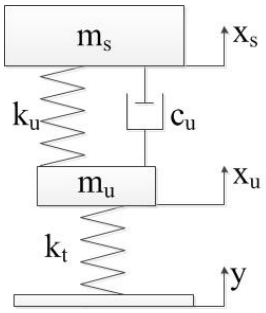

Figure 2-6. A 2-DOF quarter car model for analyzing ride comfort.

As can be seen in these equations, two important characteristics of ride quality are vertical displacement and acceleration of the sprung mass [52]. In fact, investigating the acceleration of the sprung mass and root mean square (RMS) of the acceleration is a proper way to judge the ride comfort of a vehicle. Other than its magnitude, the duration of the vertical acceleration imposed to the body is also crucial to study, given that human body is very sensitive to specific frequencies (such as those in the range of 0.5-0.75 Hz, which can cause dizziness, as can be seen in Figure 2-7) [1].

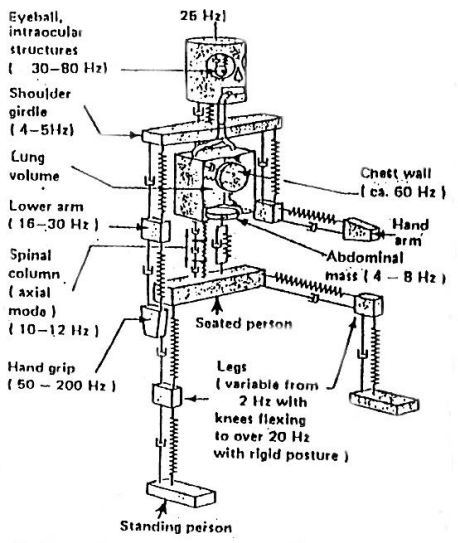

Figure 2-7. Sensitivity of different parts of human body to frequencies [7].

Importance of ride comfort has led researchers and engineers to perform ride comfort analysis for almost all types of vehicles, such as SUVs, small three wheelers, regular sedans, etc. For instance, a comprehensive 6-DOF model has been recently derived by Naidu et al. [53] in order to obtain vertical dynamic response, damped frequencies, and damped ratios for a three-wheeled vehicle (longitudinal speed was set to 45 km/h). As a matter of fact, in designing a suspension system and in the way to improve the ride comfort of a vehicle, the most important factor that has to be primarily considered is the type of the vehicle. For instance, for a small vehicle, the design of the suspension system is not only depending on the ride comfort required from the vehicle, but also on the geometrical properties of the vehicle. In case of a compact SUV, for example, it has been reported that what was restricting the design of the suspension system was the design of the chassis and also seat structure [54].

In improving the ride comfort of a vehicle, one should also bear in mind that ride comfort and handling cannot come together, simultaneously. This is simply because to have a good handling, stiff springs and high damping modes are needed. On the other hand, to have a comfortable ride, soft springs and low damping ratios are required. In this connection, for off-road vehicles, Els et al. [6] suggested a system that can switch from a good handling to a comfortable ride and vice versa.

2.4 Problem definition

In this project, dynamics of a 3-wheel, tadpole vehicle is studied. The vehicle is an all-wheel drive and steer, equipped with an active camber control. Effect of camber angle on the yaw rate at different speeds will be studied and lateral stability of the vehicle will be investigated by analyzing its rollover and skidding at various situations. Specifications of the vehicle for simulation are listed in Table 2-1.

Table 2-1. Vehicle specifications used in numerical analysis of this work

Total mass (*m*)	900 kg	**Front tire cambering stiffness ($c_{\gamma f}$)**	25000 N/rad
Front tire cornering stiffness ($c_{\alpha f}$)	25000 N/rad	**Rear tire cambering stiffness ($c\gamma_r$)**	40000 N/rad
Rear tire cornering stiffness ($c_{\alpha r}$)	40000 N/rad	**Mass moment of inertia about *z axis* (I_z)**	492 kg.m^2
Distance from front wheels to CG (*a*)	0.8 m	**Distance from CG to ground (*H*)**	0.5 m
Distance from rear wheels to CG (*b*)	1 m	**Tire radius (*r*)**	0.28 m
Sprung mass (m_s)	750 kg	**Unsprung mass of each module (m_u)**	50 kg
Spring stiffness for each front corners (k_{sf})	12000 N/m	**Vertical stiffness of tire for the rear module (k_{tr})**	230000 N/m
Spring stiffness for the rear corner (k_{sr})	16000 N/m	**Vertical stiffness of tire for each front module (k_{tf})**	230000 N/m
Damping coefficient for the rear corner (C_{sr})	2000 N.s/m	**Mass moment of inertia about *x* (I_x)**	210 kg.m^2
Damping coefficient for each front corner (C_{sf})	1200 N.s/m	**Mass moment of inertia about *z* (I_y)**	480 kg.m^2
Vehicle length (*l*)	1.8 m		

Furthermore, ride comfort of the three-wheeled vehicle will be investigated. The forces applied to the suspension joints will be also determined and analyzed. Both static and dynamic analysis will be carried out for the calculation of such forces (see Figure 2-8). Multibody Dynamics Adams software is used for the dynamic force calculations.

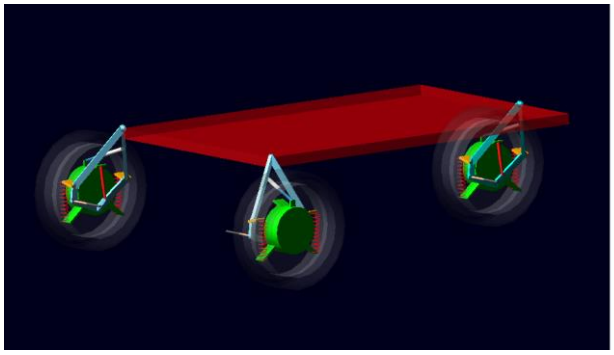

Figure 2-8. Schematic of the three-wheeled vehicle in Multibody Dynamics Adams software.

Chapter 3. Handling and Stability Analysis

In this chapter, the effects of applying camber angles on the handling and stability of the three-wheeled vehicle will be studied. Using a 3-DOF model, the transfer functions of yaw rate to camber angle and to the moment about the z axis (M_z) are derived and their effects at different speeds have been determined. In order to determine the lateral stability of vehicle, on the other hand, the effect of the camber angle on rollover of the three-wheeled vehicle is studied. The effect of road/tire friction coefficient on skidding of the vehicle is also investigated. In this connection, it will be shown that at different cambering conditions and with different road/tire coefficients, which one of the rollover or skidding will happen first.

3.1 Vehicle handling

In this section, steady state part of handling quality will be discussed in order to shed light on the effects of changing camber angle on the handling of the three-wheeled vehicle. A 3-DOF handling model will be considered. Lateral velocity (v), yaw rate (r) and roll angle (φ) of the sprung mass are considered as the degrees of freedom, as shown in Figure 2-3 and Figure 3-1.

3.1.1 A three-degree-of-freedom (3-DOF) model

In the current study, a 3-DOF model, where lateral velocity, yaw rate, and roll angle are the degrees of freedom, is considered. All transfer functions of yaw rate/camber angle and those of yaw rate/M_z of each wheel are obtained and their bode diagrams are discussed accordingly.

The handling model of the three-wheeled vehicle is schematically shown in Figure 3-1. All the equations are extracted from Newton's law. All wheels are independently steerable while camber angles can be applied to all wheels, separately.

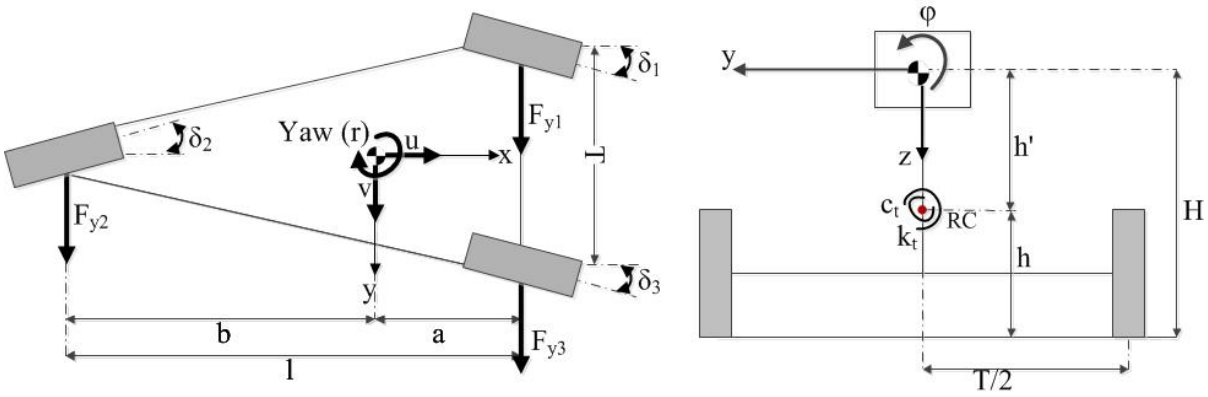

Figure 3-1. Handling model of the three-wheeled vehicle by showing degrees of freedom (lateral speed, yaw rate, and roll angle).

The general equations of motion with respect to the axes fixed to the vehicle body can be considered as (see Figure 3-1)

$$F_{y1} + F_{y2} + F_{y3} = m(\dot{v} + ur) \tag{3-1}$$

and

$$a\left(F_{y1} + F_{y3}\right) - bF_{y2} + M_z = I_z\dot{r} \tag{3-2}$$

Also

$$I_x\ddot{\varphi} + c_t\dot{\varphi} + (k_t - m_s gh)\varphi = -m_s h'(\dot{v} + ur) \tag{3-3}$$

where lateral forces on front tires are

$$F_{y1} = c_{\alpha 1}\alpha_1 + c_{\gamma 1}\gamma_1 \tag{3-4}$$

and

$$F_{y3} = c_{\alpha 3}\alpha_3 + c_{\gamma 3}\gamma_3 \tag{3-5}$$

while, lateral force on the rear wheel is

$$F_{y2} = c_{\alpha 2}\alpha_2 + c_{\gamma 2}\gamma_2 \tag{3-6}$$

F_{y1}, F_{y2}, and F_{y3} are lateral forces on each tire, m is the total weight of the vehicle and m_s is the sprung mass. Slip angles, α_1, α_2, and α_3, are derived according to the corresponding steer angles of each tire

(δ_1, δ_2, and δ_3), yaw rate (r), lateral speed (v), and longitudinal speed (u) (see below). I_z which can be seen in Equation (3-2) and I_x, appeared in Equation (3-3), are the mass moment of inertia of the vehicle, respectively, about the z and x axis (see Figure 2-3). M_z is the control moment which can be produced by torque vectoring, active steering, or their combination.

Side slip angles are defined by the vehicle motion variables such as yaw rate, longitudinal, and lateral velocity, and also according to their corresponding steer angles. Slip angle for the front wheels can be determined from

$$\alpha_1 = \delta_1 - \left(\frac{v + ar}{u}\right) \tag{3-7}$$

and

$$\alpha_3 = \delta_3 - \left(\frac{v + ar}{u}\right) \tag{3-8}$$

whereas, for the rear wheel, it can be obtained from

$$\alpha_2 = \delta_2 - \left(\frac{v - br}{u}\right) \tag{3-9}$$

By plugging Equations (3-4), (3-5), (3-6), (3-7), (3-8), and (3-9) into Equations (3-1) and (3-2), we have

$$c_{\alpha 1}\delta_1 - c_{\alpha 1}\left(\frac{v + ar}{u}\right) + c_{\gamma 1}\gamma_1 + c_{\alpha 3}\delta_3 - c_{\alpha 3}\left(\frac{v + ar}{u}\right) + c_{\gamma 3}\gamma_3 + c_{\alpha 2}\delta_2 - c_{\alpha 2}\left(\frac{v - br}{u}\right) + c_{\gamma 2}\gamma_2 = M\left(\dot{v} + ur\right) \tag{3-10}$$

while,

$$c_{\alpha 1}\delta_1 a - c_{\alpha 1}\left(\frac{v + ar}{u}\right)a + c_{\gamma 1}\gamma_1 a + c_{\alpha 3}\delta_3 a - c_{\alpha 3}\left(\frac{v + ar}{u}\right)a + c_{\gamma 3}\gamma_3 a - c_{\alpha 2}\delta_2 b + c_{\alpha 2}\left(\frac{v - br}{u}\right)b - c_{\gamma 2}\gamma_2 b + M_z = I_z\dot{r} \tag{3-11}$$

Equations (3-3), (3-10), and (3-11) are basically the expanded forms of equations of motion model for the handling analysis of the three-wheeled vehicle where $c_{\gamma 1}$, $c_{\gamma 2}$,*and* $c_{\gamma 3}$ are the camber coefficients for the front left wheel, rear wheel, and front right wheel, respectively, and $c_{\alpha 1}$, $c_{\alpha 2}$ and $c_{\alpha 2}$ are the cornering coefficients for the front left wheel, rear wheel, and front right wheel, respectively. These equations will be employed to find the state-space model.

Considering the fact that the model is linear, it is essential to use a state-space equation in order to analyze the dynamic behavior of the system. In general, a state-space equation can be written as $\dot{X} = AX + Bn$, where A is a matrix which specifies the system characteristics, B is a matrix showing how the system input affects its state, and n is the input of the system defined by

$$n = \begin{bmatrix} M_z \\ \gamma_1 \\ \gamma_2 \\ \gamma_3 \\ \delta_1 \\ \delta_2 \\ \delta_3 \end{bmatrix} \quad \textbf{(3-12)}$$

where γ_1, γ_2, and γ_3 are the camber angles applied to the front left wheel, rear wheel, and front right wheel, respectively, δ_1, δ_2, and δ_3 are the corresponding steer angles shown in Figure 3-1. The state vector (X) is defined as

$$X = \begin{bmatrix} v \\ r \\ \varphi \end{bmatrix} \quad \textbf{(3-13)}$$

The output in general can be written as $Y = CX + Dn$. In this equation, C is a matrix determining the relationship between the output and the states of the system. In the problem in hand, C is a 3×3 identity matrix. In addition, D is the feed-forward matrix that allows the input to change the output directly. In this project, since there is no feed-forward, a zero matrix D is considered.

In the following, the impact of cambering on yaw and rollover stability is studied. Therefore, the transfer functions are defined and analyzed.

3.2 Transfer functions and bode diagrams for handling analysis

In principle, transfer functions can be employed to characterize the input-output relationships of components or systems which can be defined by linear, time-invariant, differential equations. Transfer function for a system of such properties is basically defined as the ratio of the Laplace transform of the output (i.e., response function) to the Laplace transform of the input (i.e., driving function), when all initial conditions are considered zero, as described by [55]

$$\text{Transfer function} = G(s) = \frac{\ell[\text{output}]}{\ell[\text{input}]} \tag{3-14}$$

It should be noted that transfer functions are based on the nature of the system itself, while they are independent of the magnitude of the input [55].

The handling model derived in the previous section has three degrees of freedom: lateral velocity, yaw rate, and roll angle. However, since the aim of this study is to determine the effect of applying camber angle on the vehicle handling, transfer functions for the outputs of yaw rate to the inputs of camber angle and momentum will be calculated. The momentum is considered because while an external momentum (M_z) can be applied to the vehicle in order to control the yaw rate of the system, it can be also produced by traction difference in the wheels, as is the case in the current system. Seven inputs to the system will be considered: three camber angles on all wheels, three steer angles on all wheel, and a moment.

For a state-space model, the transfer function of a single-output to a single-input is

$$G(s) = C(sI - A)^{-1}B + D \tag{3-15}$$

the transfer functions of the yaw rate to the camber angle of the left front wheel and the right front wheel become

$$G_{r/\gamma 1} = G_{r/\gamma 3} = \frac{c_{\gamma 1}c_{\alpha 3}(a+b)u}{(I_z c_{\alpha 1} + I_z c_{\alpha 2} + I_z c_{\alpha 3} + a^2 c_{\alpha 1} m + a^2 c_{\alpha 2} m + b^2 c_{\alpha 3} m)us + a^2 c_{\alpha 1}c_{\alpha 3} + a^2 c_{\alpha 2}c_{\alpha 3} + b^2 c_{\alpha 1}c_{\alpha 3} + b^2 c_{\alpha 2}c_{\alpha 3} + 2abc_{\alpha 1}c_{\alpha 3} + c_{\alpha 2}c_{\alpha 3}} \tag{3-16}$$

The transfer function for the output of yaw with the input of the camber angle of the rear wheel is

$$G_{r/\gamma 2} = \frac{-c_{\gamma 2}c_{\alpha 3}(a+b)u}{(I_z c_{\alpha 1} + I_z c_{\alpha 2} + I_z c_{\alpha 3} + a^2 c_{\alpha 1} m + a^2 c_{\alpha 2} m + b^2 c_{\alpha 3} m)us + a^2 c_{\alpha 1} c_{\alpha 3} + a^2 c_{\alpha 2} c_{\alpha 3} + b^2 c_{\alpha 1} c_{\alpha 3} + b^2 c_{\alpha 2} c_{\alpha 3} + 2abc_{\alpha 1} c_{\alpha 3} + c_{\alpha 2} c_{\alpha 3}} \quad \textbf{(3-17)}$$

On the other hand, the effect of yaw rate for the moment (M_z) can be determined from

$$G_{r/M_z} = \frac{(c_{\alpha 1} + c_{\alpha 2} + c_{\alpha 3})u}{(I_z c_{\alpha 1} + I_z c_{\alpha 2} + I_z c_{\alpha 3} + a^2 c_{\alpha 1} m + a^2 c_{\alpha 2} m + b^2 c_{\alpha 3} m)us + a^2 c_{\alpha 1} c_{\alpha 3} + a^2 c_{\alpha 2} c_{\alpha 3} + b^2 c_{\alpha 1} c_{\alpha 3} + b^2 c_{\alpha 2} c_{\alpha 3} + 2abc_{\alpha 1} c_{\alpha 3} + c_{\alpha 2} c_{\alpha 3}} \quad \textbf{(3-18)}$$

Now that the transfer functions are determined, the corresponding bode diagrams can be plotted after substituting each value in the equations. A bode diagram basically includes two graphs: one is the logarithmic magnitude of a sinusoidal transfer function and the other is the phase angle. In this study, bode diagrams will be calculated for different longitudinal speeds. According to Figure 3-2 and Figure 3-3, at low frequencies, the effect of camber angle on yaw rate is more significant at higher speeds, given that the magnitude of the bode diagram is increasing. It can be also seen that the effect of camber angle on yaw rate is more elaborate for the rear wheel, in comparison to the front wheels, while at high frequencies, the camber angle effects on yaw rate (at different speeds) are almost similar. It should be noted that in practice, the frequency at which the camber angle can be changed is limited (by the actuator) under 10 rad/sec.

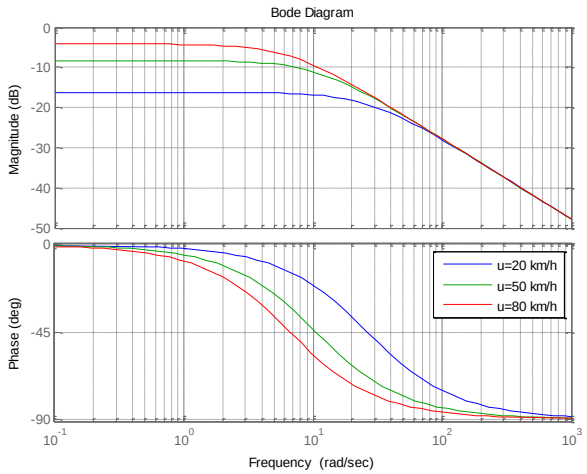

Figure 3-2. Bode diagram of the (output) yaw rate with the (input) front wheels camber angles at different vehicle speeds.

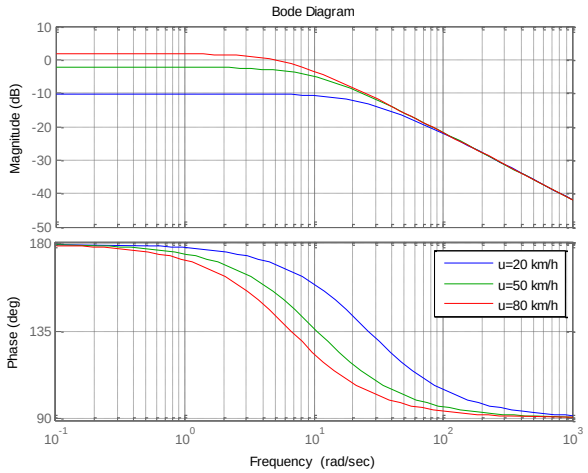

Figure 3-3. Bode diagram of the (output) yaw rate with the (input) rear wheel camber angles at different vehicle speeds.

According to Equation (3-2), the effect of applying camber angle on the yaw rate for the rear wheel is more significant, in comparison to those of the front wheels. This is simply because the rear wheel has larger distance to the vehicle CG position, in comparison to the front wheels. In fact, in order to enlarge the yaw rate values, direction of the rear camber angle should be negative, while those of the front wheels should be positive. To decrease the yaw rate, on the other hand, the opposite should be done.

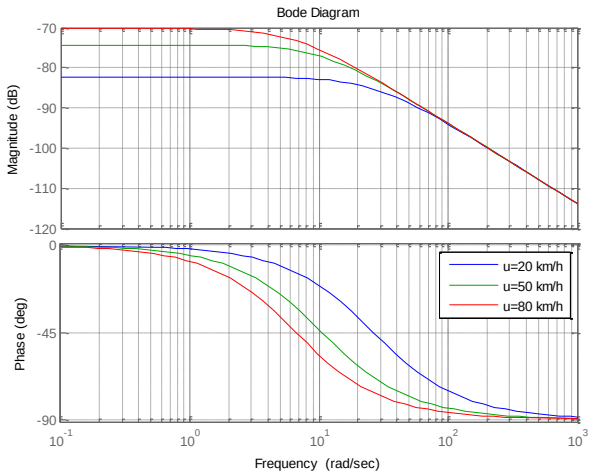

Figure 3-4. Bode diagram of the output yaw rate and the input of the corrective M_z at different vehicle speeds.

According to Figure 3-4, it can be also stated that at higher frequencies, changing the speed does not affect the yaw rate magnitude (regardless of the momentum), while at lower frequencies, by increasing the vehicle speed, the effect of this moment on yaw rate increases.

3.3 Lateral stability

One of the most important criteria in vehicle design is certainly improving the vehicle stability. In other words, during a sever maneuver, having lateral stability is important to keep the vehicle on its track. In this section, the effect of cambering on the three-wheeled vehicle rollover and skidding will be discussed in detail.

3.3.1 Rollover

In order to increase the rollover threshold of the three-wheeled vehicle, different analytical approaches are employed and the obtained results are compared with each other to better understand the advantages and disadvantages of each method. In particular, in order to increase the rollover threshold, three methods are considered. The first one is adding one positive camber to one of the front wheels and one negative camber to the other. In the second approach, two negative cambers are

applied to both front wheels while, in the third method, a camber angle is applied to the rear wheel at the same time. After obtaining the results from these three methods, the obtained results will be compared.

In sever conditions (e.g., fast steering and harsh braking), rollover or skidding could happen, which will be further studied in the following for the particular case of the three-wheeled vehicle.

3.3.1.1 Rollover threshold

In order not to risk the driver and passengers to experience rollover, it is important to know what criterion can influence rollover and investigate ways to improve that. To analyze rollover threshold, the approach used in this study is to derive an equation with zero moment about the rollover axis (see Figure 3-5). Two coordinate systems have been included. The old coordinate system in Figure 3-5 is *xy*, while the new one is called *XY*, which has been defined to simplify the calculations (see below).

At the moment just before the rollover happens, the normal force on the inner wheel should be zero, which means the inner tire is about to separate from the ground. To start with, finding the moment about the rollover axis (i.e., the line connecting the center of the outer wheels) is needed. The moment of force vector $\vec{F}$ about unit vector $\vec{e}$ is defined as

$$M = \vec{e}.(\vec{r} \times \vec{F}) \qquad \textbf{(3-19)}$$

where $\vec{e}$ is a unit vector which defines the direction of the roll axis (Equation (3-20)), while $\vec{r}$ (see Equation (3-21)) is the distance vector between force vector ($\vec{F}$) (see Equation (3-22)) and $\vec{e}$.

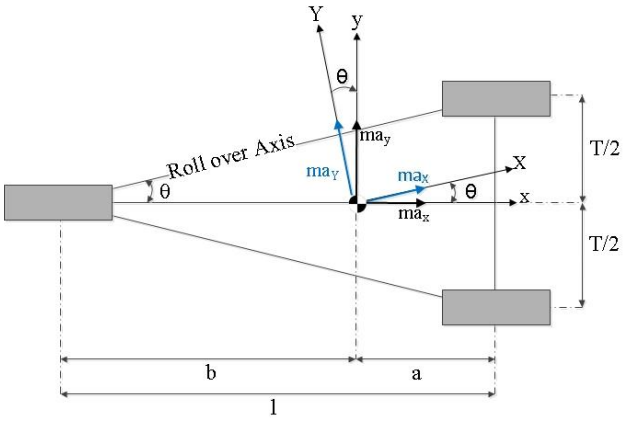

Figure 3-5. New coordinate system after a rotation about the *z* axis.

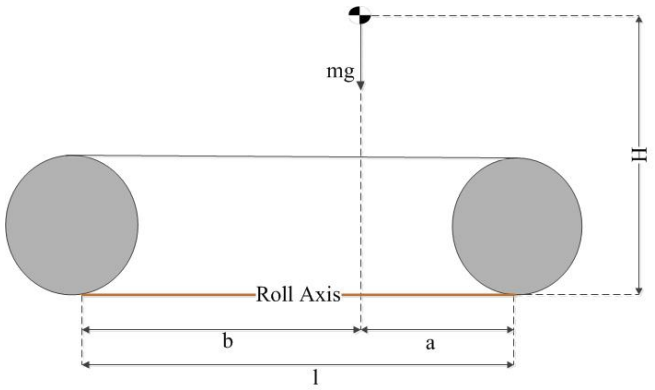

Figure 3-6. Side-view of the vehicle showing the vertical force (weight).

$\overrightarrow{F}$ is specified based on D'Alembert's principle as an inertia force acting on the sprung mass as shown parametrically in Equation (3-22).

$$\vec{e} = e_i \vec{i} + e_j \vec{j} + e_k \vec{k} \quad \textbf{(3-20)}$$

$$\vec{r} = r_i \vec{i} + r_j \vec{j} + r_k \vec{k} \quad \textbf{(3-21)}$$

$$\vec{F} = F_i \vec{i} + F_j \vec{j} + F_k \vec{k} \quad \textbf{(3-22)}$$

Being so, Equation (3-23) can be written as

$$M = \begin{bmatrix} e_i & e_j & e_k \\ r_i & r_j & r_k \\ F_i & F_j & F_k \end{bmatrix} \quad \textbf{(3-23)}$$

In order to make Equation (3-20) simpler, the new coordinate system (which is on CG location) should become parallel to the rollover axis in order to make $e = 1i$. To do so, the coordinate system should be rotated around the *z* axis for an angle θ, as shown in Figure 3-5. According to Figure 3-7, θ can be determined from

$$\theta = \tan^{-1}(\frac{T}{2l}) \quad \textbf{(3-24)}$$

Based on the new coordinate system, lateral and longitudinal forces, respectively, ma_Y, ma_X, and ma_Z are defined again as

$$ma_Y = ma_y \cos\theta - ma_x \sin\theta \quad \textbf{(3-25)}$$

$$ma_X = ma_x \cos\theta + ma_y \sin\theta \quad \textbf{(3-26)}$$

and

$$ma_Z = mg \quad \textbf{(3-27)}$$

In this new coordinate system, the roll axis is parallel to *X*. To determine the distance vector, the lateral distance from CG to rollover axis is calculated below using Figure 3-7.

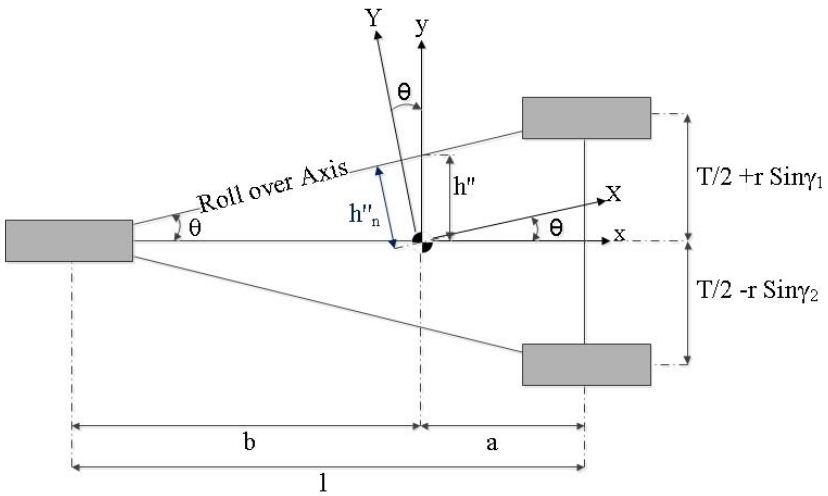

Figure 3-7. Lateral distance from CG to rollover axis.

Basically,

$$\frac{h''}{T/2} = \frac{b}{l} \quad \rightarrow \quad h'' = \frac{T \times b}{2l} \tag{3-28}$$

while

$$h''_n = h'' \cos\theta \tag{3-29}$$

By substituting Equation (3-31) in Equation (3-29), it can be stated that

$$h''_n = \frac{T \times b}{2l} \cos\theta \tag{3-30}$$

Therefore, the distance vector of Equation (3-21) can be determined from

$$\vec{r} = 0\vec{i} + h''_n \vec{j} + H\vec{k} \tag{3-31}$$

Moreover, by substituting Equation (3-30) in Equation (3-31), the final distance vector is derived as

$$\vec{r} = 0\vec{i} + \frac{T \times b}{2l} \cos\theta \, \vec{j} + (H)\vec{k} \tag{3-32}$$

In order to find the moment about the rollover axis, replacing Equations (3-25)-(3-32) in Equation (3-32) and considering $\vec{e} = 1\vec{i}$ is needed. Doing so, the rollover moment about the rollover axis can be determined from

$$M_{rollover1} = \begin{bmatrix} 1 & 0 & 0 \\ 0 & \frac{T \times b}{2l} \cos\theta & H \\ (m a_x \cos\theta + m a_y \sin\theta) & (m a_y \cos\theta - m a_x \sin\theta) & mg \end{bmatrix} \tag{3-33}$$

Therefore, when this momentum is zero,

$$\left(\frac{T \times b}{2l} \cos\theta\right)(mg) - H\,(m a_y \cos\theta - m a_x \sin\theta) = 0 \tag{3-34}$$

the corresponding a_y is considered as the rollover threshold of the vehicle and can be determined from

$$a_y = \frac{\frac{Tb}{2l} g \cos\theta + H a_x \sin\theta}{H \cos\theta} \quad \textbf{(3-35)}$$

Equation (3-35) shows the magnitude of the rollover threshold, considering the case where no camber and no roll angle has been applied to the body. By assuming zero longitudinal acceleration, rollover threshold (using the vehicle parameters in Table 2-1) will be equal to 0.78 g.

3.3.1.2 Rollover threshold study considering one negative and one positive camber angle on front wheels

One way to apply camber angle on front wheels is to apply a negative camber on one wheel and a positive camber to the other wheel. Using this approach, one basically increases the track length by adding $rSin(\gamma_1)$. It should be noted that r is not necessarily the tire radius. In some suspension systems, the position that camber is applied to the tire is not exactly at the center of the wheel. In this case, it is more accurate to consider r as the fulcrum wheel point where camber is imposed to the wheel. In general, the fulcrum wheel point can be either smaller or larger than the radius of the tire.

In principle, the goal of increasing track wheel is to add the length of torque arm that is involved in rollover analysis. As can be seen in Figure 3-8, h'' is larger in comparison to the case where there is no cambering (the term that added to the torque arm of the rollover calculation), which can cause an increase in lateral acceleration. New θ (i.e., θ_n) can then be calculated based on new changes in Equation (3-24) as

$$\theta_n = \tan^{-1}\left(\frac{\frac{T}{2} + r\sin\gamma_1}{l}\right) \quad \textbf{(3-36)}$$

Therefore, h'' in Figure 3-8 can be defined as

$$h'' = \frac{\left(\frac{T}{2} + r\sin\gamma_1\right) b}{l} \cos\theta_n \quad \textbf{(3-37)}$$

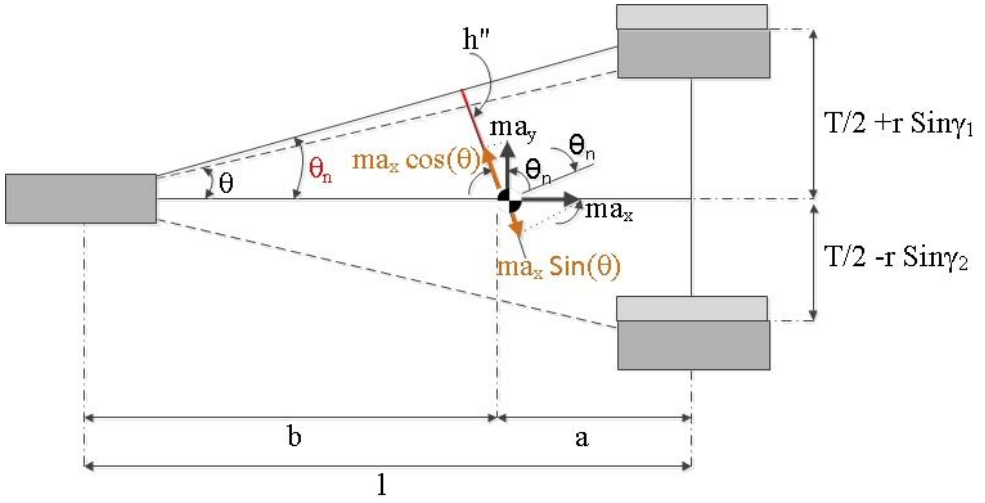

Figure 3-8. An increase in torque arm of rollover calculation upon cambering.

There are other effects on the system when camber is applied to the wheels, which causes CG position displacements, both laterally and vertically. Rollover calculations are also affected by the CG position changes in the vertical direction. From this perspective, a roll effect has been considered as a term in the analysis. Figure 3-9, schematically shows this effect.

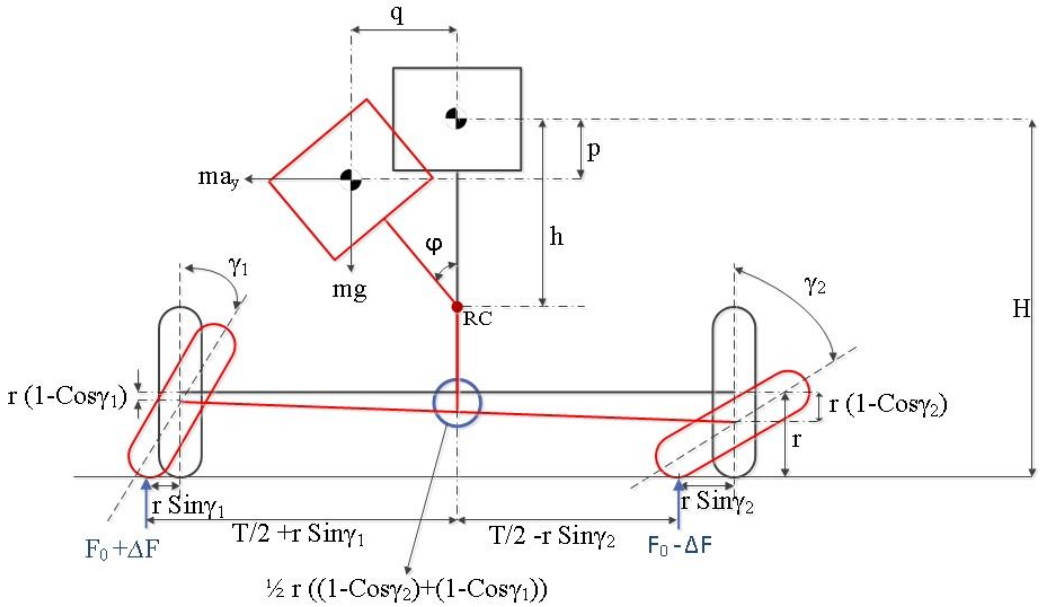

Figure 3-9. CG position changes upon applying one positive and one negative camber angle to the front wheels.

The lateral difference in CG position caused by cambering is negligible, and just the effect of roll on the body is calculated, which can be obtained from

$$q = h\ Sin\varphi \tag{3-38}$$

In this connection, the vertical difference in CG position can be calculated from

$$p = h(1-\cos\varphi) + \frac{rb}{2l}((1-\cos\gamma_2) + (1-\cos\gamma_1)) \tag{3-39}$$

Having a roll angle to the body makes it move towards the outside of the turn. This basically implies that $hsin\varphi$ should be taken into account when calculating the distance vector ($\vec{r}$). In addition, applying camber angle also causes h'' to increase, which accordingly changes the vector $\vec{r}$ to

$$\vec{r} = 0\vec{i} + \left[\frac{(T + 2r\sin\gamma_1)\times b}{2l}\cos\theta_n - h\sin\varphi\right]\vec{j} + \left[H - (h(1-\cos\varphi) + \frac{1}{2}r((1-\cos\gamma_2) + (1-\cos\gamma_1))\right]\vec{k} \tag{3-40}$$

From this perspective, the moment matrix (M_x) can be found from

$$M_{rollover2} = \begin{bmatrix} 1 & 0 & 0 \\ 0 & m_{22} & m_{23} \\ m_{31} & m_{32} & m_{33} \end{bmatrix} \tag{3-41}$$

$$m_{22} = \frac{(T + 2r\sin\gamma_1)\times b}{2l}\cos\theta_n - h\sin\varphi$$

$$m_{23} = H - (h(1-\cos\varphi) + \frac{1}{2}r((1-\cos\gamma_2) + (1-\cos\gamma_1))$$

$$m_{31} = (m a_x \cos\theta_n + m a_y \sin\theta_n)$$

$$m_{32} = (m a_y \cos\theta_n - m a_x \sin\theta_n)$$

$$m_{33} = m g$$

Accordingly, rollover threshold can be found from Equation (3-41) by knowing that the threshold starts when $M_{rollover2}$ is zero; therefore,

$$m_{22} \times m_{33} - m_{32} \times m_{23} = 0 \tag{3-42}$$

Hence, the new rollover threshold by having camber angles applied to the front wheels, and also roll angle (φ) to the body (because of the centrifugal force) caused by turning, can be estimated by

$$a_y = \frac{(T + 2r\sin\gamma_1)b\,g\cos\theta_n - 2lh\sin\varphi\,g}{(H - (h(1-\cos\varphi) + \frac{1}{2}r((1-\cos\gamma_2) + (1-\cos\gamma_1))))\cos\theta_n 2l} + \frac{a_x \sin\theta_n}{\cos\theta_n} \quad \textbf{(3-43)}$$

As demonstrated in Equation (3-43), roll angle plays a very significant role in the calculations. When having lateral acceleration (ma_y), based on the D'Alembert's principles, an external force (inertial force) is produced at the CG of the sprung mass in the direction opposite to the turn, which imposes the body to roll (Figure 3-10).

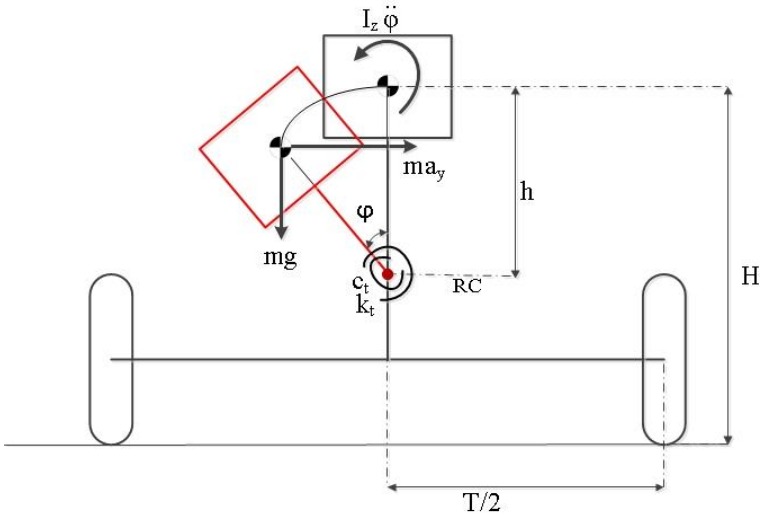

Figure 3-10. Roll angle and forces upon applying one positive and one negative camber angle to the front wheels.

From this perspective, roll dynamic equation can be obtained from

$$-m a_y h\cos\varphi + mgh\sin\varphi - k_t\varphi - c_t\dot{\varphi} = I_z\ddot{\varphi} \quad \textbf{(3-44)}$$

By considering a very small roll angle, however, it can be considered that $\sin\varphi=\varphi$ and $\cos\varphi=1$. By substituting these assumptions in Equation (3-44), we have

$$I_z\ddot{\varphi} + (mgh - k_t)\varphi + c_t\dot{\varphi} = -m a_y h \quad \textbf{(3-45)}$$

Hence, in order to find the roll angle, a steady state condition should be applied to Equation (3-45), which means $\dot{\varphi} = \ddot{\varphi} = 0$ and, as a result, it becomes

$$\left|\varphi_{ss}\right| = \frac{m a_y h}{k_t - m g h} \quad \textbf{(3-46)}$$

At this stage, the strategy is first to find a_y without applying any roll angle, by using Equation (3-43), and then calculating the roll angle that happens in that lateral acceleration, and again recalculating the lateral acceleration threshold by using its roll angle equivalent.

Table 3-1. The effect of applying different camber angles on front wheels while having positive and negative camber angles.

Lateral acceleration threshold	Camber angle outer wheel (deg)	Camber angle inner wheel (deg)	Cambering and not cambering difference in terms of threshold
0.75g	0	0	0.0 %
0.78g	5	5	4.5 %
0.82g	10	10	9.5 %
0.87g	15	15	14.6 %
0.93g	20	20	19.7 %

As can be seen in Table 3-1, the calculation results demonstrate that by increasing camber angle which was applied to the front wheels upon moving the vehicle with a constant speed, the lateral acceleration threshold increases as well. Camber angle can cause a small increment in wheels track. Equation (3-35) shows that there is a direct relationship between lateral acceleration threshold and track length. However, as track length (T) increases, lateral acceleration increases as well (see Equations (3-43) and (3-35)). Another factor which causes increasing in lateral acceleration threshold is the angle (θ) between the line that attaches the rear wheel to the front and the line that passes longitudinally through the middle of the vehicle. By increasing camber angle, θ increases, leading to an increase in the lateral acceleration threshold.

3.3.1.3 Rollover threshold study considering two negative cambers applied to front wheels

Following the one negative/one positive camber study, at this stage, it will be investigated what will happen to the lateral acceleration threshold when both front tires are having negative cambering. To start with, the lateral and longitudinal differences in CG position are calculated, both leading to completely similar results as those obtained in one negative/one positive camber angles, as described in Equation (3-43) (schematic diagram is shown in Figure 3-11).

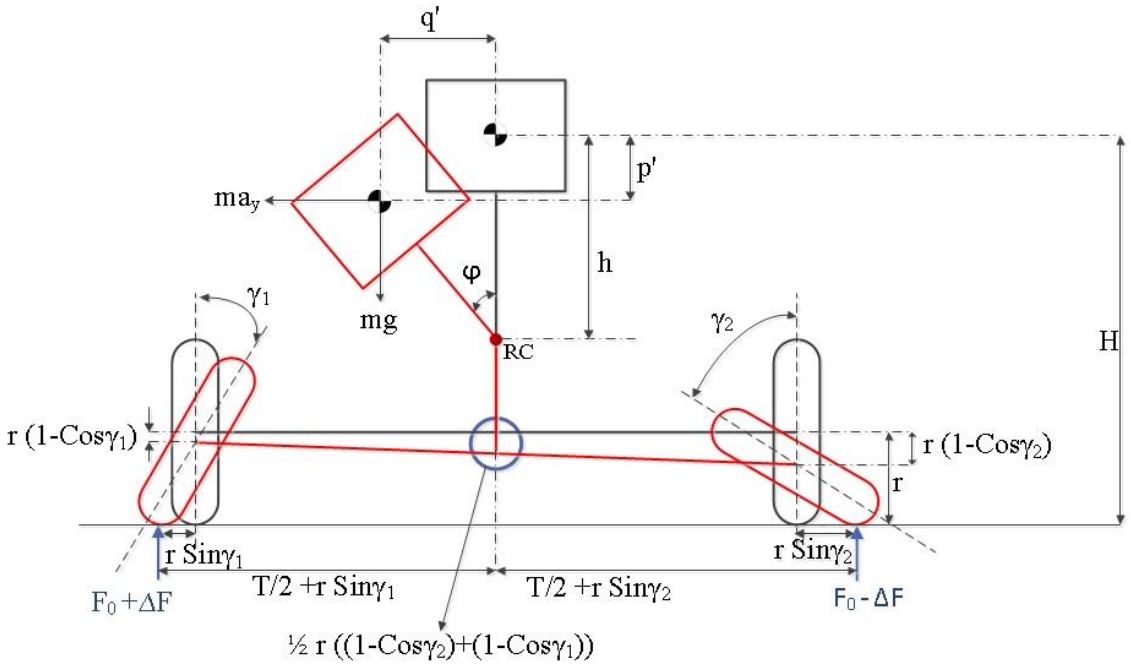

Figure 3-11. CG position change by applying negative camber angles to the front wheels.

All steps for the previous method are applicable to this method as well, because the part of the free-body diagram that we are dealing with is the upper triangle shown in Figure 3-12.

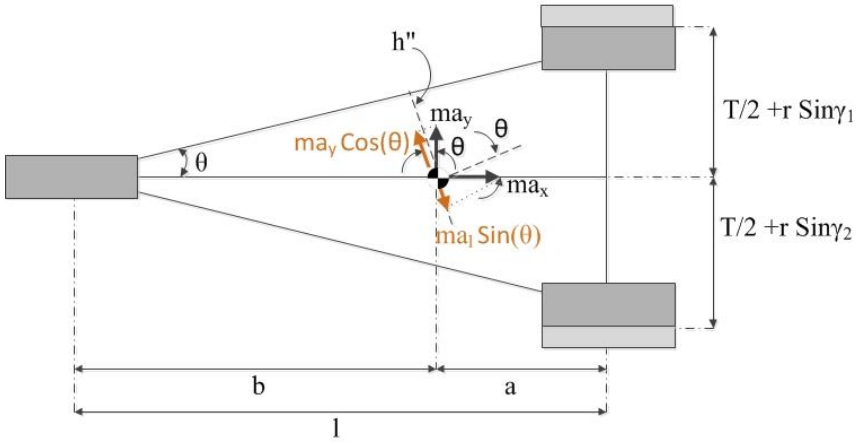

Figure 3-12. Free body diagram for the case where negative camber angles are applied to the front wheels.

Overall, it can be stated that applying negative camber angles on both front wheels leads to the lateral acceleration threshold similar to the case when there is one negative and one positive camber angle.

3.3.1.4 Rollover threshold study considering all wheels cambering

In principle, camber for the rear wheel can be applied in the same direction as the front-inner wheel or opposite to that. However, when camber angle is applied in the same direction as that of the front-outer wheel, as clearly demonstrated in Figure 3-13, the torque arm distance decreases, causing a reduction in lateral acceleration threshold. Therefore, in this study, rear wheel camber will be kept similar as that of the front inner wheel.

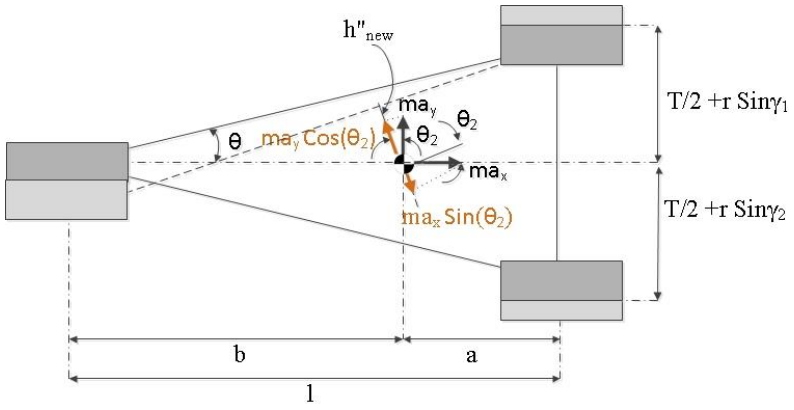

Figure 3-13. Reduction in torque arm about the rollover axis while applying an improper camber angle to the rear wheel.

When a proper camber angle direction is applied to the rear wheel, the torque arm length increases, leading to improvement in lateral acceleration threshold (as shown in Figure 3-14 for h''_{new} and free-body diagram). However, upon cambering of all wheels, the vertical CG position changes from the case where front wheels are cambered, although the effects of camber angle on its lateral changes is negligible. Vertical CG position change can be demonstrated by

$$p_{new} = h(1-\cos\varphi) + \frac{rb}{2l}((1-\cos\gamma_2)+(1-\cos\gamma_1)) + r(1-\cos\gamma_3) \tag{3-47}$$

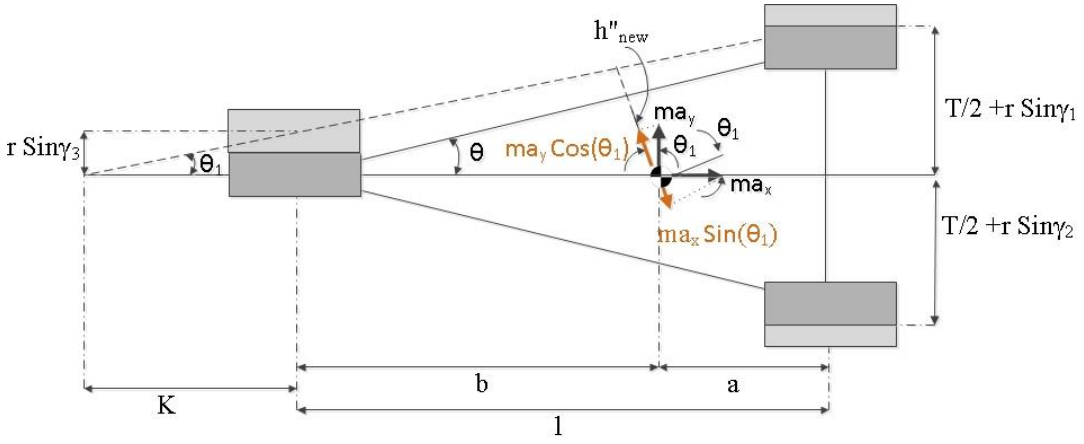

Figure 3-14. Changes in the torque arm about the rollover axis while all wheels are cambered.

As can be seen, the track length is the same as that of the front wheels. In fact, θ and the virtual length (K) are changed. K has been considered only to determine the corresponding θ. K can be determined from

$$K = \frac{lr\sin\gamma_3}{\frac{T}{2} + r(\sin\gamma_1 - \sin\gamma_3)} \tag{3-48}$$

According to Figure 3-14, θ converts to θ_1 for this new system, because of the rear camber, while its value can be obtained from

$$\theta_1 = \tan^{-1}\left(\frac{\frac{T}{2} + r\sin\gamma_1}{l + K}\right) \tag{3-49}$$

Therefore, the matrix $M_{rollover3}$ and its corresponding elements, can be determined from

$$M_{rollover3} = \begin{bmatrix} 1 & 0 & 0 \\ 0 & m_{22} & m_{23} \\ m_{31} & m_{32} & m_{33} \end{bmatrix} \quad \textbf{(3-50)}$$

$$m_{22} = \frac{(T + 2r\sin\gamma_1)\times b}{2(l+K)}\cos\theta_1 - h\sin\varphi$$

$$m_{23} = h(1-\cos\varphi) + \frac{rb}{2l}((1-\cos\gamma_2) + (1-\cos\gamma_1)) + r(1-\cos\gamma_3)$$

$$m_{31} = (m a_x \cos\theta_1 + m a_y \sin\theta_1)$$

$$m_{32} = (m a_y \cos\theta_1 - m a_x \sin\theta_1)$$

$$m_{33} = m g$$

while, the rollover threshold can be found from

$$a_y = \frac{(T + 2r\sin\gamma_1) b\, g\cos\theta_1 - 2(l+K)h\sin\varphi\, g}{(H - (h(1-\cos\varphi) + \frac{rb}{2l}((1-\cos\gamma_2) + (1-\cos\gamma_1)) + r(1-\cos\gamma_3))\cos\theta_1 2(l+K)} + \frac{a_x\sin\theta_1}{\cos\theta_1}$$

(3-51)

Figure 3-14 shows that by adding a camber angle to the rear wheel in a proper direction, practical torque arm (h''_{new}) increases. As a result, larger lateral force is needed to initiate the vehicle rollover. Table 3-2 demonstrates in detail the effects of applying camber angles on all wheels (the magnitude of the camber angle is considered similar for all cases).

Table 3-2. The effects of applying different camber angles on all wheels based on Figure 3-14.

Lateral acceleration threshold	Camber angle outer wheel (deg)	Camber angle inner wheel (deg)	Camber angle rear wheel (deg)	Cambering and not cambering difference in terms of threshold
0.75g	0	0	0	0 .0%
0.80g	5	5	5	7.1 %
0.86g	10	10	10	13.7 %
0.93g	15	15	15	19.6 %
1.00g	20	20	20	25.2 %

According to Table 3-2, by increasing the magnitude of camber angle on all wheels in the aforementioned directions, the lateral acceleration threshold increases as well. The effect of all wheels cambering on lateral acceleration threshold is more pronounced than the effect of cambering on just front wheels. This is simply due to the fact that the arm torque for the threshold is larger for the case of all-wheel cambering. The difference in length (i.e., *K*, see Figure 3-14), which comes into account only for all-wheel cambering, produces a more significant improvement in lateral acceleration threshold.

Figure 3-15 is a visual aid for comparing Table 3-1 with Table 3-2, where the slopes of the lines clearly demonstrate the acceleration threshold sensitivity to increasing camber angle. As can be seen, the slope of the red line, which corresponds to the lateral acceleration threshold for the all-wheel cambering case, is larger than the blue one, which belongs to the lateral acceleration threshold for the case of front-wheel cambering. At the maximum camber angle (i.e., 20 deg), the threshold of the red line is 1.00 g while that of the blue line is 0.93 g.

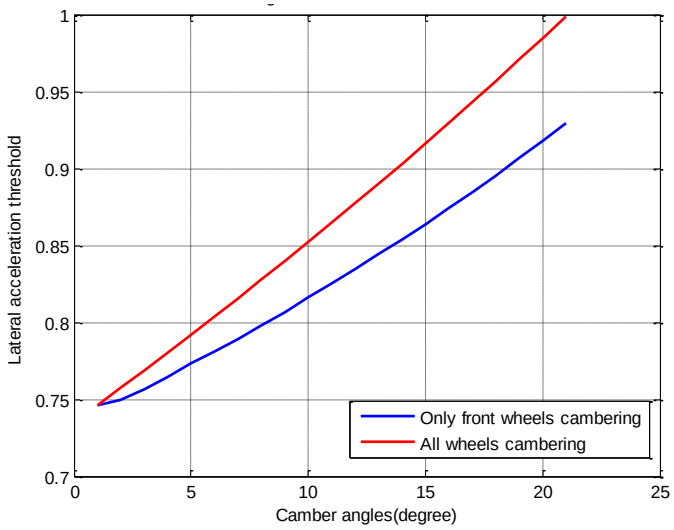

Figure 3-15. Lateral acceleration threshold vs. camber angle when all wheels and only two front wheels are cambered.

3.3.1.5 Three-wheeled geometry and rollover threshold

The tadpole geometry of the three-wheeled vehicle of this study, having two wheels in front, has its own advantages and disadvantages. As fully explained earlier, one advantage is increasing the rollover threshold upon turning and braking. In general, during a harsh turn or a maneuver, most

people tend to push the brake pedal. With this tadpole geometry, braking upon turning is actually a positive behaviour, given that upon braking, a new term is produced which is helping the vehicle not to rollover. When there is no longitudinal braking or accelerating and the vehicle is moving with a constant velocity, the force term, $ma_y\cos\theta$, makes the car to roll. Upon breaking, however, according to D'Alembert's principle, another term will be added to the lateral force, which is in the opposite direction to the vehicle acceleration direction (Figure 3-16). This new force (F_{Dy}) can be calculated from

$$F_{Dy} = m a_y \cos\theta - m a_x \sin\theta \tag{3-52}$$

which demonstrates a decline in the amount of the lateral force by $ma_x\sin\theta$, meaning larger force values are needed to make the vehicle to rollover.

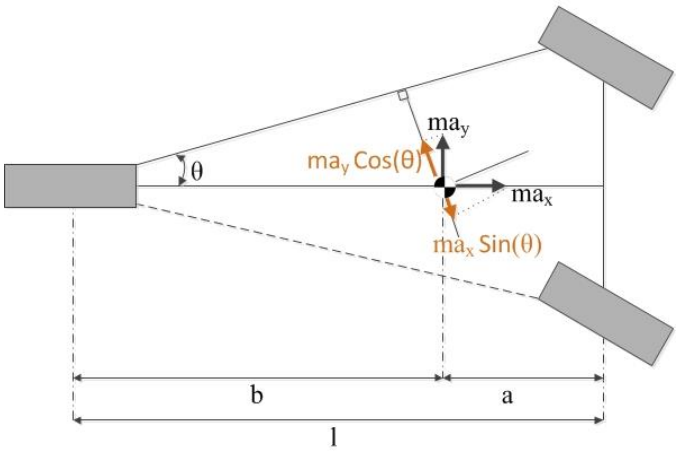

Figure 3-16. Reduction in the lateral force which makes the vehicle rollover.

An opposite result occurs when the vehicle is accelerating. The $ma_x\sin\theta$ term helps the car to turn over sooner. In fact, the tadpole design has the benefit of higher rollover threshold during braking, while the delta design has the benefit of higher rollover threshold during accelerating.

3.3.2 Skidding Study

In the previous subsection, rollover acceleration threshold and the effect of cambering were studied. In this section, the impact of cambering on skidding will be investigated. According to Rajamani [5], skid lateral acceleration threshold, based on Figure 3-17 can be found from

$$\Sigma F_z = m a_{y(\text{skidding})} \quad \textbf{(3-53)}$$

which can be expanded as

$$\mu F_{z1} + \mu F_{z2} + \mu F_{z3} = m a_{y(\text{skidding})} \quad \textbf{(3-54)}$$

where μ is the road/tire coefficient of friction while F_{z1} , F_{z2}, and F_{z3} are vertical forces on the front-right, rear, and front-left wheel, respectively . This equation can also be simplified in the form of

$$\mu m g = m a_{y(\text{skidding})} \quad \textbf{(3-55)}$$

which basically gives

$$\mu g = a_{y(\text{skidding threshold})} \quad \textbf{(3-56)}$$

The free body diagram corresponding to this system is shown in Figure 3-17.

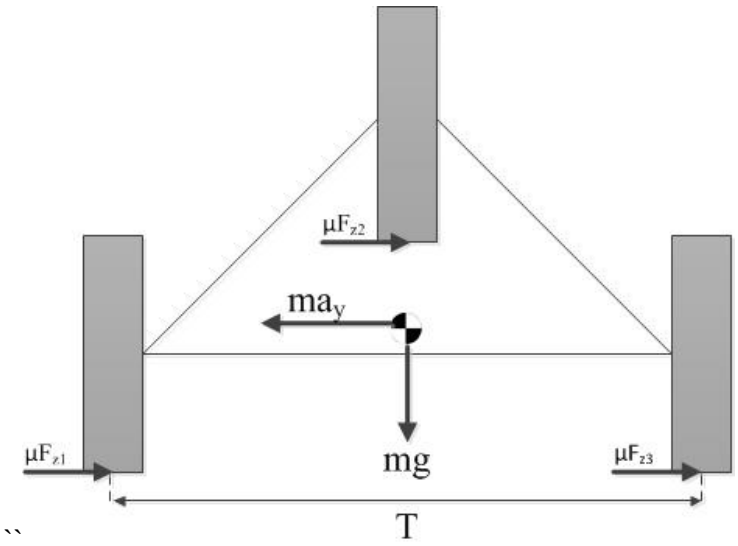

Figure 3-17. Free body diagram for skidding.

According to Equation (3-56), the skidding lateral acceleration threshold directly depends on the road/tire friction coefficient, μ, and gravity acceleration (g), meaning that it has nothing to do with the geometry of the vehicle and also its weight. Skidding for various road/tire friction situations is calculated (see Table 3-5 and Table 3-6).

Assuming there is no roll angle and based on Equation (3-35), the skidding lateral acceleration for all road types (see Table 3-3) are found and the results are outlined in Table 3-4.

Table 3-3. Road/tire friction coefficient for different types of roads [56].

Road Type	Road/tire friction coefficient (μ)
Dry	0.90
Wet	0.60
Snowy	0.20
Icy	0.05

When camber angle was not applied to the wheels while there is no roll angle, rollover lateral acceleration magnitude is determined to be 0.78 g on all different road types. However, skidding totally depends on friction coefficient. As can be seen in Table 3-4, rollover happens sooner than skidding while driving on dry roads. This happens because rollover threshold magnitude is less than its equivalent in skidding.

Table 3-4. Skidding lateral acceleration threshold for the case of no camber, no roll.

Road Type	Road/tire friction coefficient (μ)	Rollover lateral acceleration threshold	Skidding lateral acceleration threshold
Dry	0.90	0.78g	0.90g
Wet	0.60	0.78g	0.60g
Snowy	0.20	0.78g	0.20g
Icy	0.05	0.78g	0.05g

Naturally, either rollover threshold or skidding threshold has a smaller amount than the other one. In dry roads, with 0.90 road/tire coefficient of friction, with camber angles smaller than 20 deg, rollover happens because its threshold magnitude is smaller than the corresponding skidding value. In all other cases as seen in Table 3-5, skidding happens before rollover.

Table 3-5. Skidding lateral acceleration threshold when different camber angles are applied to the front wheels while having different road/tire friction coefficients.

Road Type	Road-tire friction coefficient (μ)	Camber angle (deg)	Rollover lateral acceleration threshold (Front wheels camber)	Skidding lateral acceleration threshold (Front wheels camber)
Dry	0.9	0	0.75g	0.90g
		5	0.78g	0.90g
		10	0.82g	0.90g
		15	0.87g	0.90g
		20	0.93g	0.90g
Wet	0.6	0	0.75g	0.60g
		5	0.78g	0.60g
		10	0.82g	0.60g
		15	0.87g	0.60g
		20	0.93g	0.60g
Snowy	0.2	0	0.75g	0.20g
		5	0.78g	0.20g
		10	0.82g	0.20g
		15	0.87g	0.20g
		20	0.93g	0.20g
Icy	0.05	0	0.75g	0.05g
		5	0.78g	0.05g
		10	0.82g	0.05g
		15	0.87g	0.05g
		20	0.93g	0.05g

When having all wheels cambering, there is the same scenario for the vehicle. In wet, snowy, and icy roads, only skidding happens, while for the case of a dry road, rollover happens with camber angles smaller than 15 deg, as can be seen in Table 3-6.

In this chapter, the effect of camber angle on yaw rate and accordingly, on the vehicle handling at various speeds was determined. It was shown that at lower frequencies, effect of camber angle on yaw rate is more significant at higher speeds. It was also determined that this effect for the rear wheel is more pronounced in comparison to the front wheels. At high frequencies, on the other hand, it was illustrated that changing the speed does not significantly affect the yaw rate.

The other aspect that was discussed in this chapter was the effect of applying different camber angles on the rollover threshold. It was illustrated that by applying negative camber angles on the outer-turn wheel, rollover threshold increases. In this case, the camber direction of the other wheel is not important. In this chapter, it was also demonstrated that at different camber angles and on different roads, skid or rollover happens. It was shown that on wet, snowy, and icy roads, the possibility of occurrence of skidding is higher than rollover. On dry roads, on the other hand, rollover mostly

happens first. However, on dry roads, when the wheels have 15 to 20 deg camber angles, the possibility of rollover and skidding are very close to each other. The MATLAB code for handling analysis and rollover threshold study can be found in Appendix A.

Table 3-6. Skidding lateral acceleration threshold when different camber angles are applied to the all wheels while having different road/tire friction coefficients.

Road type	Road/tire friction coefficient (μ)	Camber angle (deg)	Rollover lateral acceleration threshold (All-wheels camber)	Skidding lateral acceleration threshold (All-wheels camber)
Dry	0.90	0	0.75g	0.90g
		5	0.80g	0.90g
		10	0.86g	0.90g
		15	0.93g	0.90g
		20	1.00g	0.90g
Wet	0.60	0	0.75g	0.60g
		5	0.80g	0.60g
		10	0.86g	0.60g
		15	0.93g	0.60g
		20	1.00g	0.60g
Snowy	0.20	0	0.75g	0.20g
		5	0.80g	0.20g
		10	0.86g	0.20g
		15	0.93g	0.20g
		20	1.00g	0.20g
Icy	0.05	0	0.75g	0.05g
		5	0.80g	0.05g
		10	0.86g	0.05g
		15	0.93g	0.05g
		20	1.00g	0.05g

Chapter 4. Ride Comfort Analysis and the Force Measurements of the Suspension System Parts

In this chapter, ride quality comfort of the three-wheeled vehicle, having two wheels in the front and one in the back, is studied. First, an analytical model with 6-DOF is developed to determine the ride comfort parameters (i.e., vertical displacement and acceleration of the sprung mass) of the three-wheeled vehicle. For this analysis, two different types of roads, one with a single haversine bump and a sinusoidal road with multiple bumps, will be considered. Furthermore, pitch angle, vertical displacement, and acceleration generated by moving on the aforementioned roads will be calculated. Finally, transmissibility of road irregularities to the body will be estimated by determining the corresponding transfer functions.

For the suspension design, the resulting forces to the key points in the suspension system will be determined. A static and dynamic analysis will be used. In the static analysis, an acceleration of 1g for the lateral acceleration, 2g for the vertical acceleration, and 3g for the longitudinal acceleration are considered. To assure the accuracy of the results, the suspension joint forces will be also calculated (using Multibody Dynamics Adams software) by simulating the vehicle motion on different types of roads (such as over a single haversine bump and over a road with a specific roughness) at different speeds. For the particular case of moving over a haversine bump, the ride comfort parameters (such as vertical displacement and acceleration) will be obtained from both analytical and simulation methods and the advantages and disadvantages of using each method will be discussed accordingly.

4.1 Ride comfort study

One of the most important criteria for a good vehicle is the ride comfort, which basically describes how convenient and comfortable the vehicle is for the driver and passengers [57,58]. To determine the ride comfort of the three-wheeled vehicle of this study, a 6-DOF model is considered. The degrees of freedom of this model are considered to be the front-right wheel vertical displacement (x_{ufr}), front-left wheel vertical displacement (x_{ufl}), rear wheel vertical displacement (x_{ur}), sprung mass vertical displacement (x_s), pitch motion (ω), and roll motion (φ), as shown in Figure 4-1.

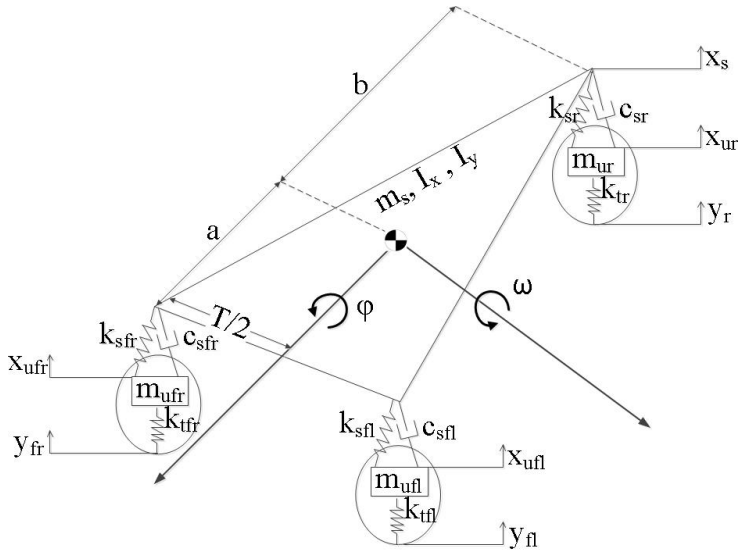

Figure 4-1. Schematic of the 6-DOF model and the degrees of freedom for ride comfort analysis of the three-wheeled vehicle.

In this model, the dynamic equation of motion for ride comfort (based on Newton's law) for the sprung mass is

$$m_s \ddot{x}_s + k_{sfl}(x_s - x_{ufl} + \frac{T}{2}\varphi - a\,\omega) + c_{sfl}(\dot{x}_s - \dot{x}_{ufl} + \frac{T}{2}\dot{\varphi} - a\,\dot{\omega}) + k_{sfr}(x_s - x_{ufr} - \frac{T}{2}\varphi - a\,\omega) \quad \textbf{(4-1)}$$

$$+ c_{sfr}(\dot{x}_s - \dot{x}_{ufr} - \frac{T}{2}\dot{\varphi} - a\,\dot{\omega}) + k_{sr}(x_s - x_{ufr} + b\,\omega) + c_{sr}(\dot{x}_s - \dot{x}_{ur} + b\,\dot{\omega}) = 0$$

where m_s is the sprung mass, k_{sfl} is the spring coefficient of the front-left suspension corner module, k_{sfr} is the spring coefficient of the front-right suspension corner module, k_{sr} is the spring coefficient of the rear suspension corner module, c_{sfl} is the damping coefficient of the front-left suspension corner module, c_{sfr} is the damping coefficient of the front-right suspension corner module, c_{sr} is the damping coefficient of the rear suspension corner module, a is the longitudinal distance from CG to the front axle, b is the longitudinal distance from CG to the rear wheel, and T is the track width. Having this, the equation of motion for roll motion can be written as

$$I_x\ddot{\varphi} + k_{sfl}\frac{T}{2}(x_s - x_{ufl} + \frac{T}{2}\varphi - a\,\omega) + c_{sfl}\frac{T}{2}(\dot{x}_s - \dot{x}_{ufl} + \frac{T}{2}\dot{\varphi} - a\,\dot{\omega})$$
$$- k_{sfr}\frac{T}{2}(x_s - x_{ufr} - \frac{T}{2}\varphi - a\,\omega) - c_{sfr}\frac{T}{2}(\dot{x}_s - \dot{x}_{ufr} - \frac{T}{2}\dot{\varphi} - a\,\dot{\omega}) = 0 \quad \textbf{(4-2)}$$

where I_x is the mass moment of inertia of the vehicle about the *x* axis. The pitch motion equation can be described as

$$I_y\ddot{\omega} - k_{sfl}\,a(x_s - x_{ufl} + \frac{T}{2}\varphi - a\,\omega) - c_{sfl}\,a(\dot{x}_s - \dot{x}_{ufl} + \frac{T}{2}\dot{\varphi} - a\,\dot{\omega}) - k_{sfr}\,a(x_s - x_{ufr} - \frac{T}{2}\varphi - a\,\omega) \quad \textbf{(4-3)}$$
$$- c_{sfr}\,a(\dot{x}_s - \dot{x}_{ufr} - \frac{T}{2}\dot{\varphi} - a\,\dot{\omega}) + k_{sr}\,b(x_s - x_{ufr} + b\omega) + c_{sr}\,b(\dot{x}_s - \dot{x}_{ur} + b\dot{\omega}) = 0$$

where I_y is the mass moment of inertia of the vehicle about the *y* axis. Unsprung mass for the front-left corner module can be calculated by

$$m_{ufl}\ddot{x}_{ufl} - k_{sfl}(x_s - x_{ufl} + \frac{T}{2}\varphi - a\,\omega) - c_{sfl}(\dot{x}_s - \dot{x}_{ufl} + \frac{T}{2}\dot{\varphi} - a\,\dot{\omega}) - k_{tfl}(x_{ufl} - y_{fl}) = 0 \quad \textbf{(4-4)}$$

while, that of the front-right corner module can be determined from

$$m_{ufr}\ddot{x}_{ufr} - k_{sfr}(x_s - x_{ufr} - \frac{T}{2}\varphi - a\,\omega) - c_{sfr}(\dot{x}_s - \dot{x}_{ufr} - \frac{T}{2}\dot{\varphi} - a\,\dot{\omega}) + k_{tfr}(x_{ufr} - y_{fr}) = 0 \quad \textbf{(4-5)}$$

Finally, the equation for the rear wheel will be

$$m_{ur}\ddot{x}_{ur} - k_{sr}(x_s - x_{ufr} + b\omega) - c_{sr}(\dot{x}_s - \dot{x}_{ur} + b\dot{\omega}) + k_{tr}(x_{ur} - y_r) = 0 \quad \textbf{(4-6)}$$

where m_{ufl} , m_{ufr}, and m_{ur} are mass of the unsprung mass for the front-left module, front-right module, and rear module, respectively. y_{fl}, y_{fr}, and y_r are the road irregularities which are applied respectively to the front-left wheel, front-right wheel, and rear wheel (see Figure 4-1).

For the dynamic analysis, Equations (4-1)-(4-6) should be modeled in a state-space form like what was done for the handling analysis (see subsection 3.1.1). Therefore, by considering the state space equation as

$$\dot{X}_{12\times1} = \begin{bmatrix} A_{c[6\times6]} & A_{k[6\times6]} \\ I_{[6\times6]} & 0_{[6\times6]} \end{bmatrix} X_{12\times1} + [B]_{12\times3}\,n_{3\times1} \quad \textbf{(4-7)}$$

where

$$A_c = \begin{bmatrix} \frac{-c_{sfl}-c_{sfr}-c_{sr}}{m_s} & \frac{-\frac{T}{2}c_{sfl}+\frac{T}{2}c_{sfr}}{m_s} & \frac{a.c_{sfl}+a.c_{sfr}-b.c_{sr}}{m_s} & \frac{c_{sfl}}{m_s} & \frac{c_{sfr}}{m_s} & \frac{c_{sr}}{m_s} \\ \frac{-\frac{T}{2}c_{sfl}+\frac{T}{2}c_{sfr}}{I_x} & \frac{-(\frac{T}{2})^2 c_{sfl}+(\frac{T}{2})^2 c_{sfr}}{I_x} & \frac{\frac{T}{2}a.c_{sfl}-\frac{T}{2}a.c_{sfr}}{I_x} & \frac{\frac{T}{2}c_{sfl}}{I_x} & \frac{-\frac{T}{2}c_{sfr}}{I_x} & 0 \\ \frac{a.c_{sfl}+a.c_{sfr}-b.c_{sr}}{I_y} & \frac{\frac{T}{2}a.c_{sfl}-\frac{T}{2}a.c_{sfr}}{I_y} & \frac{-a^2.c_{sfl}-a^2.c_{sfr}-b^2.c_{sr}}{I_y} & \frac{-a.c_{sfl}}{I_y} & \frac{-a.c_{sfr}}{I_y} & \frac{b.c_{sr}}{I_y} \\ \frac{c_{sfl}}{m_{ufl}} & \frac{\frac{T}{2}c_{sfl}}{m_{ufl}} & \frac{-a.c_{sfl}}{m_{ufl}} & \frac{-c_{sfl}}{m_{ufl}} & 0 & 0 \\ \frac{c_{sfr}}{m_{ufr}} & \frac{-\frac{T}{2}c_{sfr}}{m_{ufr}} & \frac{-a.c_{sfr}}{m_{ufr}} & 0 & \frac{-c_{sfr}}{m_{ufr}} & 0 \\ \frac{c_{sr}}{m_{ur}} & 0 & \frac{b.c_{sr}}{m_{ur}} & 0 & 0 & \frac{-c_{sr}}{m_{ur}} \end{bmatrix} \quad \textbf{(4-8)}$$

and

$$A_k = \begin{bmatrix} \frac{-k_{sfl}-k_{sfr}-k_{sr}}{m_s} & \frac{-\frac{T}{2}k_{sfl}+\frac{T}{2}k_{sfr}}{m_s} & \frac{a.k_{sfl}+a.k_{sfr}-b.k_{sr}}{m_s} & \frac{k_{sfl}}{m_s} & \frac{k_{sfr}}{m_s} & \frac{k_{sr}}{m_s} \\ \frac{-\frac{T}{2}k_{sfl}+\frac{T}{2}k_{sfr}}{I_x} & \frac{-(\frac{T}{2})^2 k_{sfl}+(\frac{T}{2})^2 k_{sfr}}{I_x} & \frac{\frac{T}{2}a.k_{sfl}-\frac{T}{2}a.k_{sfr}}{I_x} & \frac{\frac{T}{2}k_{sfl}}{I_x} & \frac{-\frac{T}{2}k_{sfr}}{I_x} & 0 \\ \frac{a.k_{sfl}+a.k_{sfr}-b.k_{sr}}{I_y} & \frac{\frac{T}{2}a.k_{sfl}-\frac{T}{2}a.k_{sfr}}{I_y} & \frac{-a^2.k_{sfl}-a^2.k_{sfr}-b^2.k_{sr}}{I_y} & \frac{-a.k_{sfl}}{I_y} & \frac{-a.k_{sfr}}{I_y} & \frac{b.k_{sr}}{I_y} \\ \frac{k_{sfl}}{m_{ufl}} & \frac{\frac{T}{2}k_{sfl}}{m_{ufl}} & \frac{-a.k_{sfl}}{m_{ufl}} & \frac{-k_{sfl}-k_{tfl}}{m_{ufl}} & 0 & 0 \\ \frac{k_{sfr}}{m_{ufr}} & \frac{-\frac{T}{2}k_{sfr}}{m_{ufr}} & \frac{-a.k_{sfr}}{m_{ufr}} & 0 & \frac{-k_{sfr}-k_{tfr}}{m_{ufr}} & 0 \\ \frac{k_{sr}}{m_{ur}} & 0 & \frac{b.k_{sr}}{m_{ur}} & 0 & 0 & \frac{-k_{sr}-k_{tr}}{m_{ur}} \end{bmatrix} \quad \textbf{(4-9)}$$

while,

$$B = \begin{bmatrix} 0 & 0 & 0 \\ 0 & 0 & 0 \\ 0 & 0 & 0 \\ \frac{k_{tfl}}{m_{ufl}} & 0 & 0 \\ 0 & \frac{k_{tfr}}{m_{ufr}} & 0 \\ 0 & 0 & \frac{k_{tr}}{m_{ur}} \\ 0 & 0 & 0 \\ 0 & 0 & 0 \\ 0 & 0 & 0 \\ 0 & 0 & 0 \\ 0 & 0 & 0 \\ 0 & 0 & 0 \end{bmatrix} \quad \textbf{(4-10)}$$

The state vector X is defined by

$$X^T = \begin{bmatrix} \dot{x}_s & \dot{\varphi} & \dot{\omega} & \dot{x}_{ufl} & \dot{x}_{ufr} & \dot{x}_{ur} & x_s & \varphi & \omega & x_{ufl} & x_{ufr} & x_{ur} \end{bmatrix} \quad \textbf{(4-11)}$$

Besides, matrix n (input for the system) is

$$n = \begin{bmatrix} y_{fl} \\ y_{fr} \\ y_r \end{bmatrix} \quad \textbf{(4-12)}$$

4.1.1 Transfer functions and bode diagrams for ride quality analysis

The transmissibility of road irregularities to the sprung mass is first discussed. This will be done by determining the ratio of the vibration magnitudes of the body to the amplitude of the road profile irregularities. Using the same methodology used to determine the transfer functions in subsection 3.2 and according to Figure 4-1, all transfer functions of sprung mass displacement for front and rear wheels are calculated. In particular, the transfer function of the vertical displacement of the sprung mass of each of the front wheels (using the vehicle parameters listed in Table 2-1) is

$$G_{\frac{x_s}{y_{fr}}} = G_{\frac{x_s}{y_{fl}}} = \frac{1.472e4s^9 + 2.068e6s^8 + 3.474e8s^7 + 2.122e10s^6 + \ldots}{s^{12} + 189.2s^{12} + 3.969e4s^{10} + 3.896e6s^9 + 3.871e8s^8 + 1.933e10s^7 + 9.747e11s^6 + \ldots}$$
$$\frac{\ldots + 1.436e12s^5 + 1.582e13s^4 + 7.92e13s^3 + 1.502e14s^2 - 1.16e14s - 1.365e14}{\ldots + 1.116e13s^5 + 7.892e13s^4 + 2.735e14s^3 + 5.228e14s^2 - 4.177e14s - 4.914e14}$$

(4-13)

The corresponding bode diagram of this transfer function can be seen in Figure 4-2, where the blue line is for the case where the ratio of unsprung mass/sprung mass is 20%, and the green line is for the case where the weight of unsprung mass is changed from 50 kg to 25 kg, resulting a ratio of unsprung mass/sprung mass of 10%. The sprung mass in both cases is 750 kg. As can be seen in the figure, there is no change in the bode diagrams at low frequencies, while at high frequencies, the lighter unsprung mass showed lower transmissibility ratio (green line). That is, with the same level of high frequency excitation, lighter unsprung mass can provide lower vibration of the sprung mass. Even so, in the range of 20 to 80 rad/sec, the lighter unsprung mass produces higher transmissibility ratios to the body, in comparison to the heavier unsprung mass.

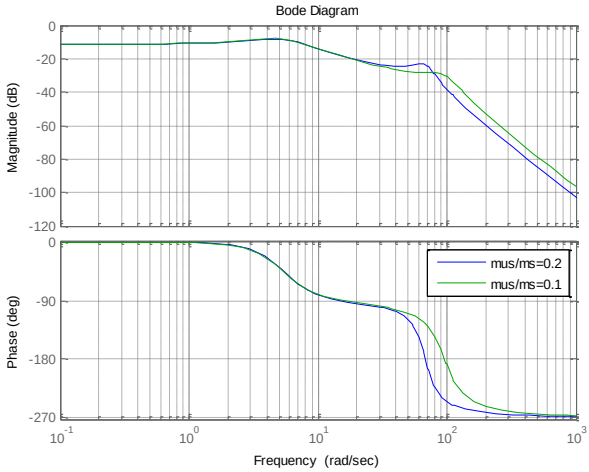

Figure 4-2. Bode diagrams of the vertical displacement/road irregularities of the front wheels.

The transfer function of the vertical displacement of the sprung mass of the rear wheel can be written as

$$G_{\frac{x_s}{y_r}} = \frac{2.453e4s^9 + 2.63e6s^8 + 5.326e8s^7 + 2.723e10s^6 + \ldots}{s^12 + 189.2s^11 + 3.969e4s^10 + 3.896e6s^9 + 3.871e8s^8 + 1.933e10s^7 + 9.747e11s^6 + \ldots}$$

$$\frac{\ldots + 2.315e12s^5 + 2.352e13s^4 + 1.272e14s^3 + 2.416e14s^2 - 1.857e14s - 2.184e14}{\ldots + 1.116e13s^5 + 7.892e13s^4 + 2.735e14s^3 + 5.228e14s^2 - 4.177e14s - 4.914e14}$$

(4-14)

In fact, the magnitude of the transfer function of the body displacement/road irregularities of the rear wheel input is larger than that of the front wheel, demonstrating that the rear wheel transfers larger magnitude of the road irregularities to the body. In Figure 4-3, it is also shown that the ratio of the unsprung mass/sprung mass does not affect the transmissibility ratio for the rear wheel as much as it does those for the front wheels, although improvements at high frequencies still exist.

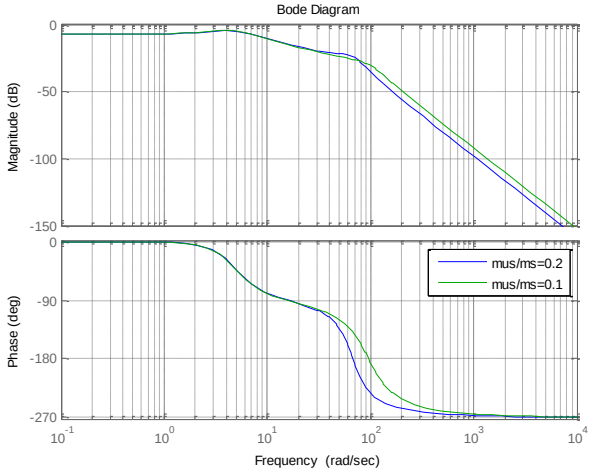

Figure 4-3. Bode diagrams of the vertical displacement/road irregularities of the rear wheel.

4.1.2 Isolated bump

Road roughness is an important criterion that affects the ride quality [59, 60]. In this section, an isolated havesine road profile is considered to study the ride comfort of the three-wheeled vehicle by determining the ride comfort parameters, including the sprung mass vertical displacement and acceleration. For a single bump, it is important to observe the way that springs and dampers reduce the vibrations which are transmitted to the body [61]. For the case of a single haversine bump, the input for the front-left wheel and the front-right wheel can be determined from

$$y_{fl} = y_{fr} = d.\mathrm{hav}(\frac{2\pi u}{L}t) \quad \textbf{(4-15)}$$

For the rear wheel, however, since there is a phase difference between front wheels and the rear wheel (which is directly proportional to the length of the car), the input should be calculated by

$$y_r = d.\mathrm{hav}(\frac{2\pi u}{L}(t+\frac{l}{u})) \quad \textbf{(4-16)}$$

where d is the height of the bump (10 cm), L is the length of the bump (100 cm), u is the longitudinal speed (assumed 20 km/h), and l is the length of vehicle (1.8 m). The haversine bump profile is shown in Figure 4-4.

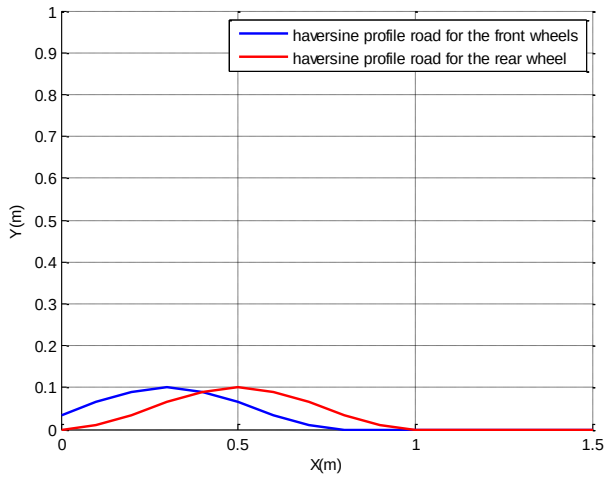

Figure 4-4. The haversine bump profiles which are applied to front wheels and the rear wheel.

As mentioned, the conventional way to analyze the ride comfort is to observe the vertical displacement of the sprung mass (car body). The vertical displacement of the three-wheeled vehicle when it passes over the haversine bump of 10 cm height is shown in Figure 4-5.

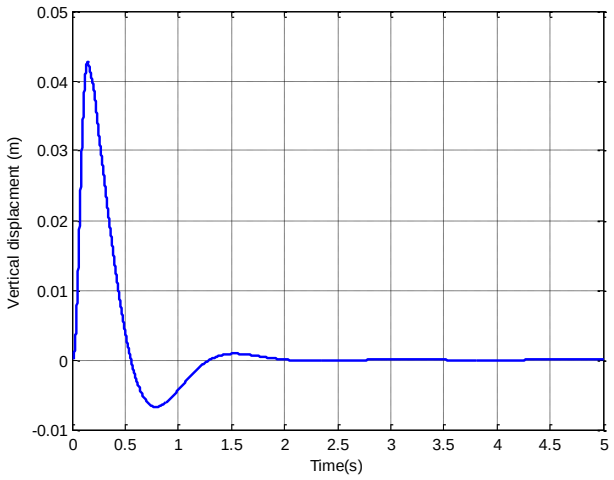

Figure 4-5. Vertical displacement of the sprung mass when the three-wheeled vehicle goes over a haverine bump of 10 cm height.

In modeling the ride comfort of the vehicle when it passes over the single haversine bump, according to the longitudinal velocity of the vehicle and also the road characteristics, the time duration for passing over the bump is calculated. As can be seen in Figure 4-5, the vertical displacement of sprung mass is damped approximately after two seconds while the maximum amplitude of oscillation transmitted to the car body is 42% of the road amplitude.

Another criterion, which should be considered when studying the ride comfort of a vehicle, is vertical acceleration of the sprung mass. Figure 4-6 shows the imposed acceleration to the sprung mass of the three-wheeled vehicle when it is passing over the haversine bump.

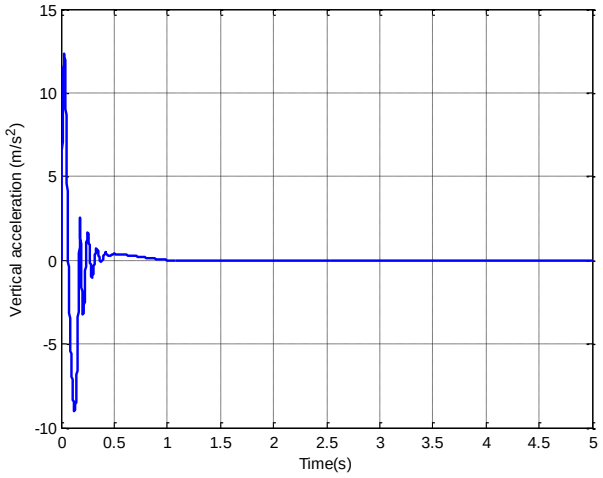

Figure 4-6. Vertical acceleration for the body when the vehicle passes over a single haversine bump.

According to Figure 4-6, the maximum acceleration imposed to the car body at the specific speed of 40 km/h is almost 13.1 m/s^2.

The pitch angle of the vehicle for the same haversine bump is shown in Figure 4-7. It is demonstrated that upon moving over the isolated bump, the body rotates around the *y* axis for less than 0.4 deg, which is satisfactory for the vehicle.

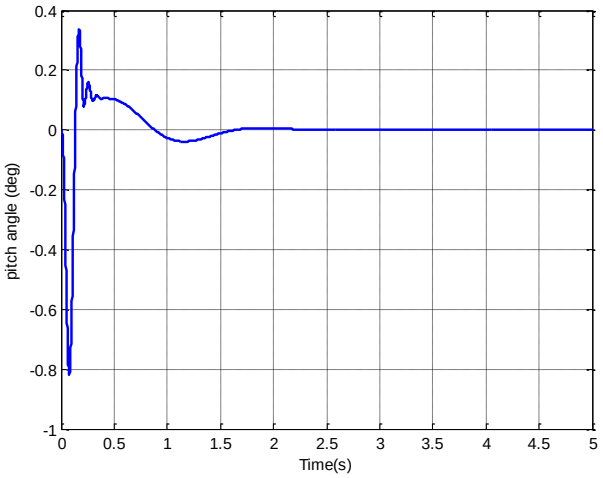

Figure 4-7. Pitch angle developed when the vehicle passes over a single haversine bump.

Thus far, the effect of moving over a single haversine bump has been studied in order to determine how it could affect the ride comfort of the vehicle. At this stage, it is necessary to investigate the behaviour of the suspension system by moving the car over multiple bumps and in particular, over a sinusoidal road.

4.1.3 Sinusoidal road

In this part, a sinusoidal road is included to see what happens to the vehicle in terms of its ride comfort when it goes over multiple bumps in a continuous fashion. The input profile for the front-left and front-right wheels will therefore be

$$y_{fl} = y_{fr} = d.\sin(\frac{2\pi u}{L}t) \quad \textbf{(4-17)}$$

For the rear wheel, however, by considering the difference phase which is the result of the difference in longitudinal direction, we have

$$y_r = d.\sin(\frac{2\pi u}{L}(t+\frac{l}{u})) \quad \textbf{(4-18)}$$

Here, same as for the haverine bump, d is the height of the bump (considered 5 cm), L is the length of each sinusoidal bump, which is 1 m, and u is 20 km/h. The road profile for all wheels can be seen in Figure 4-8.

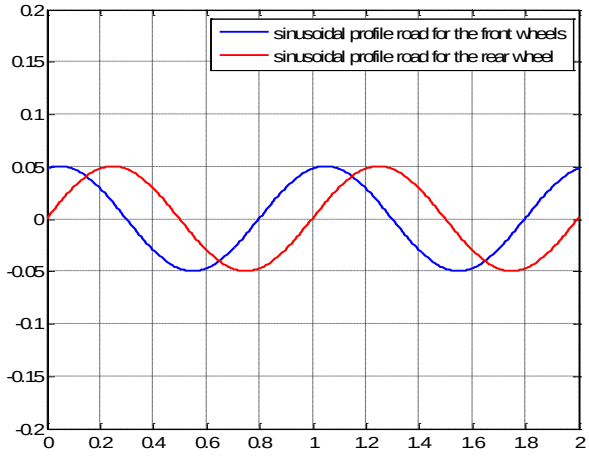

Figure 4-8. The sinusoidal road profiles which are applied to front wheels and the rear wheel.

The vertical displacement of the car body when it moves over a sinusoidal road is illustrtared in Figure 4-9. In general, the performance of a suspension system, with regard to the vehicle ride comfort, is acceptable when the transmissiblity ratio (i.e., car body displacement to height of the bump) settles down to values under 12% of the bump. As can be seen in Figure 4-9, when the three-wheeled vehicle starts to go over the first bump, transmissiblity ratios are as large as 24%. After one second, however, the system starts to oscillate between -7 mm and 7 mm. Although oscillations in this range (i.e., transmissiblity of 14%) are a little bit high, but still they are promising, given that only 14% of the road irregularities are transmitted to the body.

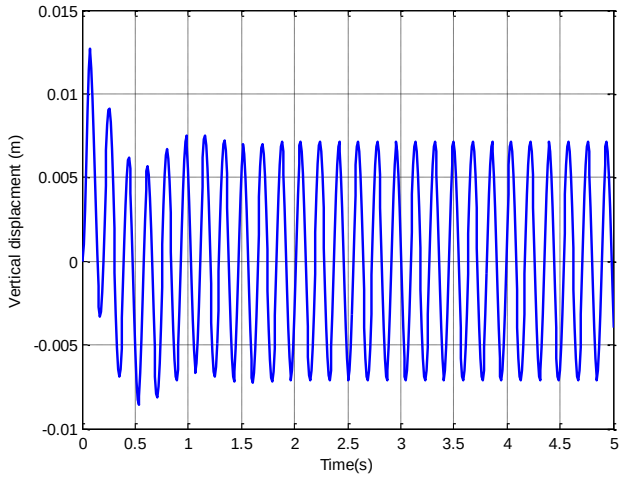

Figure 4-9. Vertical displacement of the sprung mass when the vehicle passes over a sinusoidal road.

At this point, we start to study the vertical acceleration of the vehicle body in order to determine the acceleration which is imposed to passengers and the driver. According to Figure 4-10, the maximum acceleration of the body is 12.1 m/s^2 at the very first time when the body starts to go over the first bump. After 0.25 s, however, the vertical acceleration of the system starts to oscillate between -8.7 to 8.7 m/s^2 .

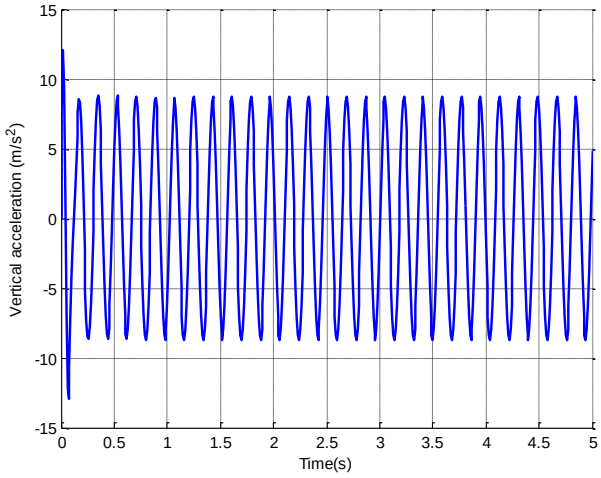

Figure 4-10. Vertical acceleration for the body when the vehicle passes over a sinusoidal road.

Figure 4-11 shows the pitch angle that occurs when the vehicle passes over the sinusoidal road. It can be seen that maximum pitch angle of ~0.7 deg is produced when the vehicle goes over the first bump and after 0.5 s, the system starts to oscillate between about -0.4 to 0.4 deg.

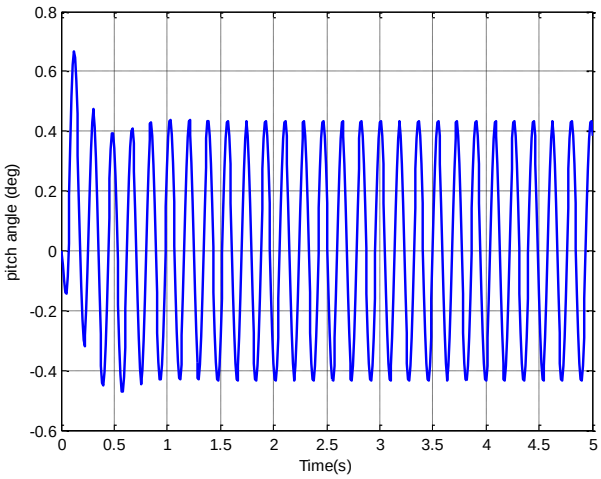

Figure 4-11. Pitch angle when the vehicle passes over a sinusoidal road.

4.2 Suspension force study: static analysis

In this part, by using Multibody Dynamics Adams software, the effect of applying maximum acceleration forces in longitudinal, vertical, and lateral directions on joints of the suspension system (when the vehicle is not moving) will be studied. By considering maximum forces at all joints, it can be studied whether the design of the suspension system is optimized or not. Besides, it can be determined that at which parts larger forces are expected to be produced.

Figure 4-12 demonstrates the name and location of each part of the in-wheel suspension system of the three-wheeled vehicle, while Table 4-1 shows the static forces developed on each part of the suspension system when the conventional 1g lateral, 2g vertical, and 3g longitudinal acceleration forces are imposed to the vehicle [62,63].

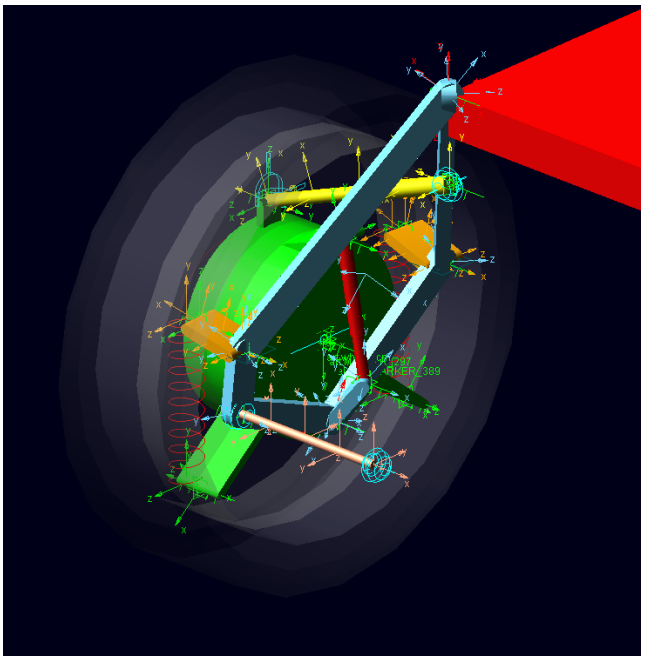

Figure 4-12. In-wheel suspension system and its components; the yellow cylinder is the camber linkage while the blue set of the links are called as the mechanism in this thesis. The peach cylinder is the steer linkage, the green part is its hub, and the red part is the body.

As demonstrated in Figure 4-12, the in-wheel suspension system of the vehicle of this study contains different parts, such as links, revolute joints, spherical joints, hook joints, springs, and a damper. Considering the fact that the design of the suspension system is not finalized yet, in this study, only forces at some of the key points of the suspension system will be studied. However, the method

employed here can be applied later to determine forces at other key points when the design of the suspension system is finalized.

Table 4-1. Forces at each part of the suspension system when maximum of 1g lateral, 2g vertical, and 3g longitudinal acceleration forces are imposed to the vehicle.

PARTS	FORCE (N)
Mechanism to body (lower one)-left	6905
Mechanism to body (lower one)-right	6038
Mechanism to body (lower one)-rear	16739
Mechanism to body (upper one)-left	2409
Mechanism to body (upper one)-right	3154
Mechanism to body (upper one)-rear	11153
Camber to body-left	12183
Camber to body-right	6056
Steer to mechanism-left	13655
Steer to mechanism-right	1795
Steer to mechanism-rear	21229

According to Table 4-1, maximum force is produced on the suspension system of the rear wheel, and particularly on the steer link that attaches mechanism of the suspension system to the body, which basically happens when the vehicle is accelerating in the longitudinal direction at 3g. This is because the rear wheel carries a larger load of the vehicle mass.

Regardless of the generated forces, one should bear in mind that in reality, either 1g lateral, 2g vertical, or 3g longitudinal acceleration are very large numbers, while they hardly happen simultaneously. It should be noted that these large force values are chosen only to have a large safety factor in design of the suspension system.

At this stage and when the static forces on the suspension system are determined, extracting all the forces at the joints by moving the vehicle on different road profiles would be necessary.

4.3 Vehicle dynamic simulation on different road profiles (Adams)

At this stage, by using Multibody Dynamics Adams software, forces that are developed at various parts of the suspension system of the three-wheeled vehicle, upon moving on roads of different profiles, will be calculated. Dynamic simulation of the behaviour of the whole vehicle helps us to know what is happening to the vehicle during different situations, while it also allows us to determine

if the design of the suspension system is optimized or not. In this study, two different road profiles will be considered. First, same as in the previous part, an isolated haversine road profile with a single bump having a large height will be considered for the analysis and forces at the joints of the suspension system will be calculated. Next, the same analysis will be carried out for two different irregular bumpy roads with multiple bumps.

4.3.1 Isolated haversine road

In this study, the height of the bump is considered 10 cm and its length is set to 1 m. The longitudinal speed of the vehicle is constant at 12 km/h.

Figure 4-13 demonstrates the force vs. time profile for the movement of the three-wheeled vehicle when passing over an isolated haversine bump. It can be seen in this figure that, in comparison to the rear wheel, smaller forces are generated at the joints of the front wheels, particularly at those attaching the mechanisms to the body. This was expected since there are two wheels in the front and one in the rear.

At t = 6 s, the vehicle goes over the bump and the impact force starts fluctuating for almost two seconds before it settles down. As shown in Figure 4-13, the maximum force generated on the lower joints attaching the body to the mechanism of the front wheels and the rear one are 6500 N and 8300 N, respectively, which are still less than those measured in the static force study (see Table 4-1).

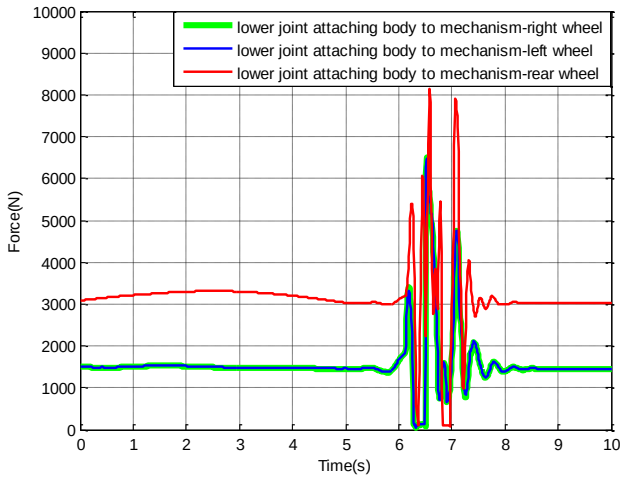

Figure 4-13. Force vs. time for haversine road profile for the lower joint attaching the body to the mechanism.

For the rear wheel, Figure 4-14 demonstrates that the maximum force happens at the rear steer joint (which is attaching to the mechanism) when the rear wheel goes over the bump (at about 7.0th second). For the front wheels, on the other hand, the maximum force is also developed when the front wheels start to go over the bump, but at about 6.5th second. It should be noted that the maximum developed forces at these joints are slightly smaller than 1500 N, which is still way below the static results.

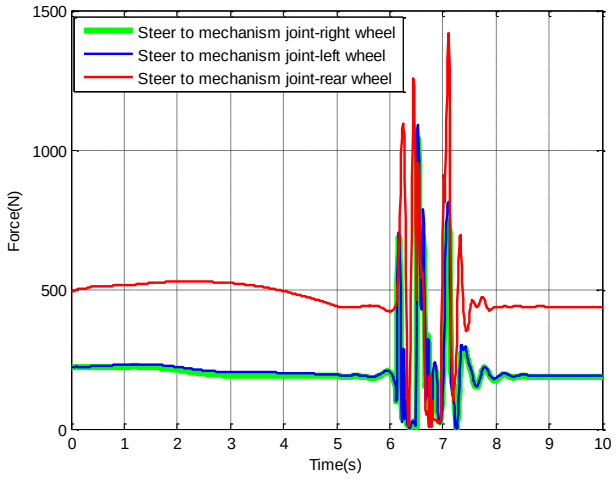

Figure 4-14. Force vs. time for haversine road profile for the steer joint attaching to the mechanism.

Figure 4-15 and Figure 4-16 illustrate the vertical displacement of the body determined from simulation (Adams) and analytical study (MATLAB), respectively. From the simulation results, it is seen that the maximum displacement over a 10 cm bump is 8.2 cm; the analytical results, however, shows a maximum displacement of 7.5 cm (at the longitudinal speed of 12 km/h). According to simulation results, at this speed, the vehicle absorbs 18% of the fluctuations caused by road irregularities, while analytical results demonstrate 25% absorption. That is, there is 7% difference between analytical and simulation results, which might be caused because of few reasons. The first reason is that all results in analytical part were obtained based on a linear model; however, the simulation software considers all nonlinearities in the system. The other reason is the tire model. In the analytical model, a linear model was considered, while in the simulation, a nonlinear Pacejka model was used.

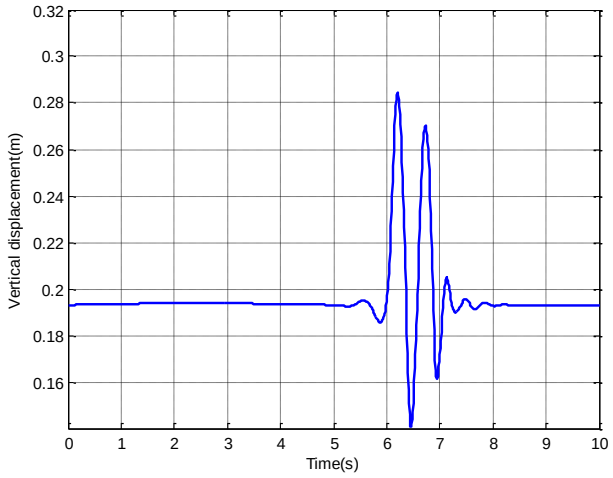

Figure 4-15. Vertical displacement of sprung mass when the vehicle passes over a haverine bump (Adams-simulation).

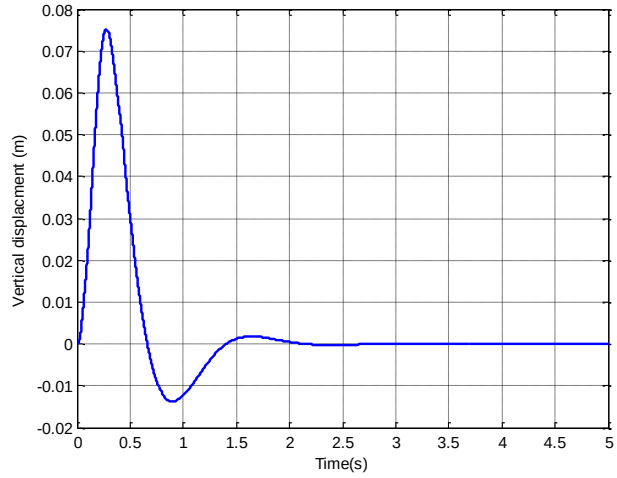

Figure 4-16. Vertical displacement of the sprung mass when the vehicle passes over a haverine bump (MATLAB-analytical).

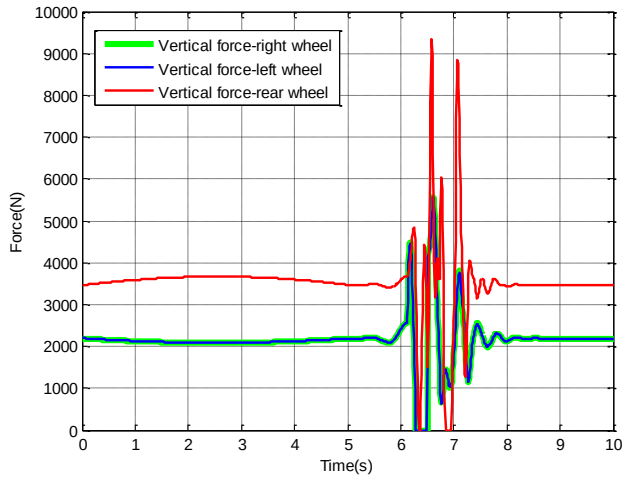

Figure 4-17. Vertical tire forces on all three wheels for an isolated haversine bump.

In the following, the forces developed on tire contact patches will be studied. In fact, tires are important parts of the unsprung mass and in order to analyze the ride comfort and durability of the vehicle over rough road profiles, it is necessary to determine the vertical forces developed on tires [64]. The vertical forces that are imposed to the tires are shown in Figure 4-17. When the vehicle is not moving, based on the CG position, each front wheel is holding 2260 N force in the vertical direction while the rear wheel is bearing 3710 N. Within the first five seconds and when the vehicle is accelerating, the load is transferred longitudinally from the front module to the back. Because of

having two wheels in front and one in rear, the load transfer has more significant impact on the rear wheel, in comparison to the front wheels. Therefore, the maximum force generated during movement on the rear wheel is 9500 N while that on each of the front wheels is only 5630 N.

Finally, effects of passing over an isolated bump on the acceleration of the vehicle will be studied and the results of the simulation will be compared with those obtained from analytical study. Analytical vertical acceleration values calculated when the vehicle is passing over a single bump is shown in Figure 4-18. As can be seen, the maximum acceleration (9.0 m/s^2) to the body happens when the front wheels start to go over the bump. On the other hand, the maximum acceleration determined from simulation is about 7.0 m/s^2, which also happens when the rear wheel goes over the bump (see Figure 4-19). As mentioned, since many terms are neglected in the analytical study, it is not very surprising that the simulation results are being slightly different from the analytical results, while they are both still in the same range.

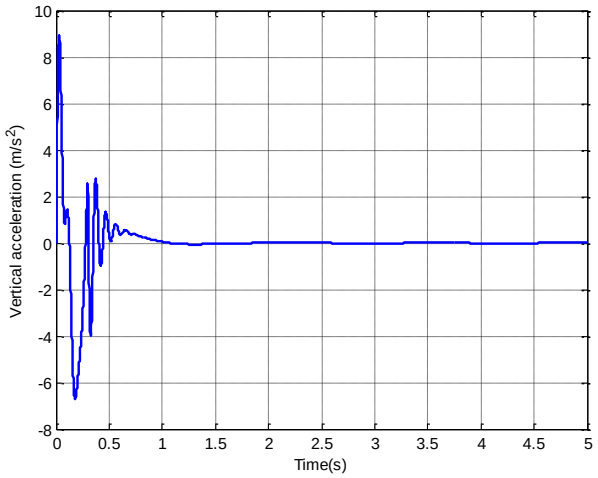

Figure 4-18. Vertical acceleration of the sprung mass when the vehicle passes over a haverine bump (MATLAB-analytical).

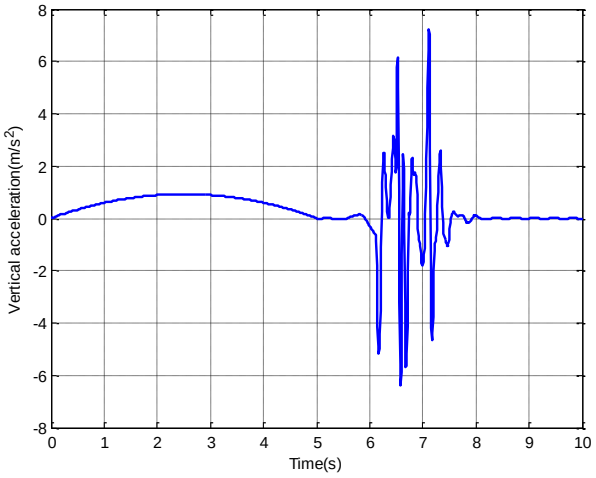

Figure 4-19. Vertical acceleration of the sprung mass when the vehicle passes over a haverine bump (Adams-simulation).

4.3.2 Simulation on rough road

Thus far, the behaviour of the three-wheeled vehicle and the forces developed at different joints of its suspension system when the vehicle was passing over a single haversine bump was studied. In the following, the vehicle is simulated on standard rough roads.

A type B road, based on the ISO standard, is selected for the simulation and a constant speed of 70 km/h is assumed for the vehicle. Figure 4-20 shows the forces for the lower joint attaching the body to the mechanism. For the first 1.4 s, the vehicle is passing over a smooth flat road. After this time, the vehicle reaches road type B, while the vehicle is still accelerating. During acceleration, significant amount of load is transferred to the rear wheel (which has a single module), and as a result, forces developed at the rear wheel at this time are larger than those formed at modules in the front. After acceleration is over, however, the vehicle moves with a constant speed of 70 km/h. At this stage, the force in the lower joint attaching the body to the mechanism of the rear wheel decreases dramatically.

During the acceleration mode, the maximum force that is generated at this joint in the rear wheel is 9023 N, while that during the constant speed mode is only 4659 N. It should be noted that the forces generated at this joint either during the acceleration or at constant speed, according to static analysis, are in the safe zone (see Table 4-1)

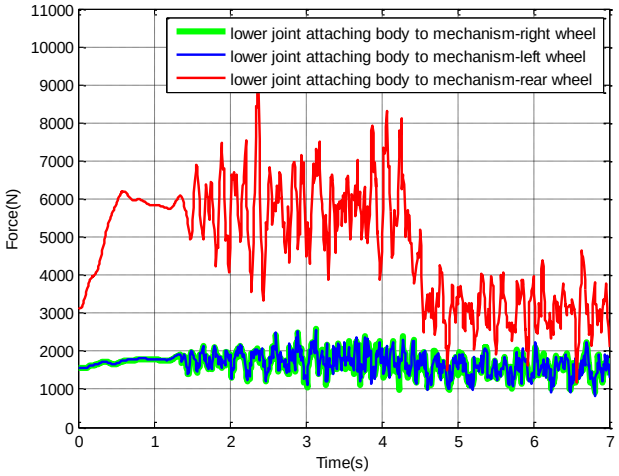

Figure 4-20. Force vs. time for road type B profile for the lower joints attaching the body to the mechanisms of wheels.

Figure 4-21 demonstrates the forces at joints attaching the steer system to the mechanism. As can be seen in this figure, larger forces are formed at the rear steer joint than the front one, especially in the first five seconds because of the vehicle acceleration. It should be noted that forces developed at the steer joints (see Figure 4-21) are still in the safe zone, as determined in the static analysis.

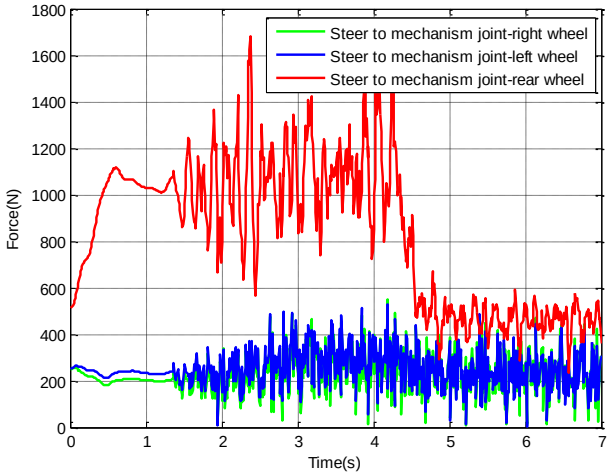

Figure 4-21. Force vs. time for the steer joints attached to mechanisms when the vehicle goes over road type B.

Figure 4-22 shows the vertical displacement of the sprung mass on road type B. As can be seen, the maximum vertical displacement of the sprung mass is 7.5 mm. Given that the maximum road roughness is set to 4 cm, it can be stated that over 80% of the displacement caused by the road is absorbed by the suspension system, when the vehicle is moving at 70 km/h.

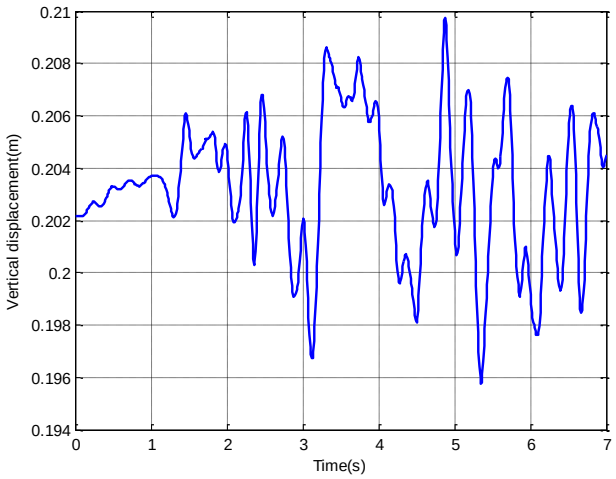

Figure 4-22. Vertical displacement of the sprung mass when the vehicle goes over road type B profile (Adams-simulation results).

In Figure 4-23, tire forces developed in the vertical direction are illustrated. It can be seen in this figure that the vertical force on the single rear tire is initially increasing (during the acceleration period), while those of the front wheels are decreasing. When the acceleration ends, however, only force fluctuations caused by road irregularities are observable. It is also worthwhile mentioning that, since the rear tire is bearing larger forces (as discussed before), fluctuations of the rear wheel is taking place in a larger force range, in comparison to those of the front wheels.

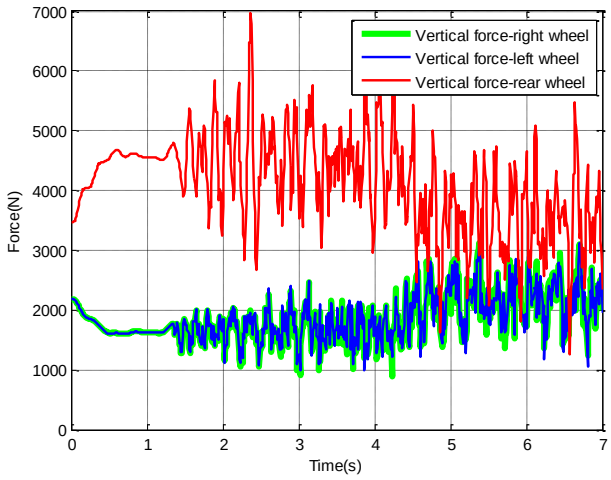

Figure 4-23. Vertical tire forces on all three wheels for road type B profile.

4.4 Simulation analysis of the dynamic behavior during simultaneous accelerating and turning (Adams)

Up to this point, effects of moving over a single bump (which had a large height) and also over a type B road were studied. In the following, the suspension joint forces are evaluated when the vehicle is accelerated while it is turning.

In this study, the vehicle acceleration time to reach 40 km/h is considered 6 s. Steer angles from 0 to 5 degrees are applied to the front wheels, and 0 to 4 degrees are applied to the rear wheel. Between the 2^{nd} and 5^{th} second, constant camber angle of 6 deg is applied to the front wheels. Figure 4-24 shows the forces for the lower joints attaching the body to the mechanism and Figure 4-25 demonstrates the same but for the upper joints. It can be seen that because of acceleration, all forces developed at joints (which are attaching mechanisms to the body) are larger, in comparison to the case where the vehicle was stationary. After 6 s, however, the forces settle down, because the vehicle moves with a constant force. In addition, it was observed that forces at the left joint and the right one are not changing in the same manner, because of load transfer due to turning. It is also worthwhile mentioning that the force discrepancies of the rear wheel are not as elaborate as those of the front suspension systems, since lateral force naturally imposes more effects on them than on the single module of the rear wheel.

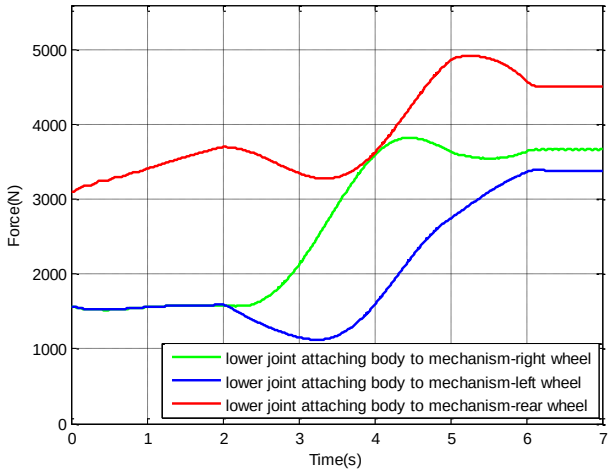

Figure 4-24. Force vs. time for the lower joints attaching the body to mechanisms when the vehicle is turning, accelerating, and cambering, at the same time.

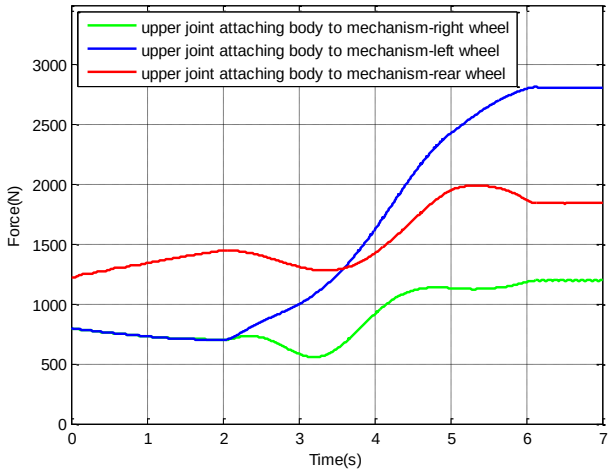

Figure 4-25. Force vs. time for the upper joints attaching the body to mechanisms when the vehicle is turning, accelerating, and cambering, at the same time.

Force vs. time diagram for the joint attaching steer links to mechanisms is shown in Figure 4-26. As being demonstrated, forces at the joint in the right module have larger forces in comparison to the other two. In fact, this has happened because this particular steer link, upon turning, imposes a force to the joint in order to move it for turning.

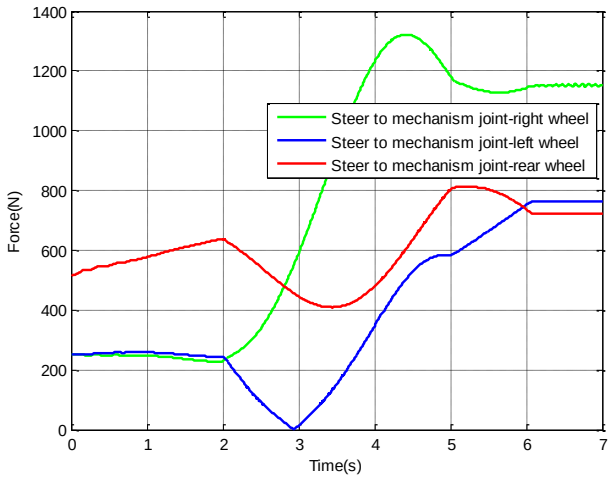

Figure 4-26. Force vs. time for joints attaching steer links to mechanisms when the vehicle is turning, accelerating, and cambering, at the same time.

However, the forces in the left joint are smaller because of the effects of lateral load transfer, which are actually happened between the 2nd and 2.9th second. Even so, after this time, the steer force in the left wheel started to rise because of the lateral load transfer due to turning. It should be also noted that there are some small fluctuations in forces of the rear joint (considering the force has been applied to the steer joint of the rear wheel as well), which should be also because of instabilities caused by the longitudinal and lateral load transfers.

Forces for the joints securing camber links to the suspension systems can be seen in Figure 4-27. Again, due to longitudinal load transfer, reductions in the forces of both front joints are observed in the first 2.5 s (for the right wheel) and 3.2 s (for the left one). After these times, because the camber angles are applied (starting at the 2nd s), both forces start to increase. It is worthwhile mentioning that since the vehicle is turning at the same time, lateral load transfer happens, which in turn causes the increase in the right wheel forces.

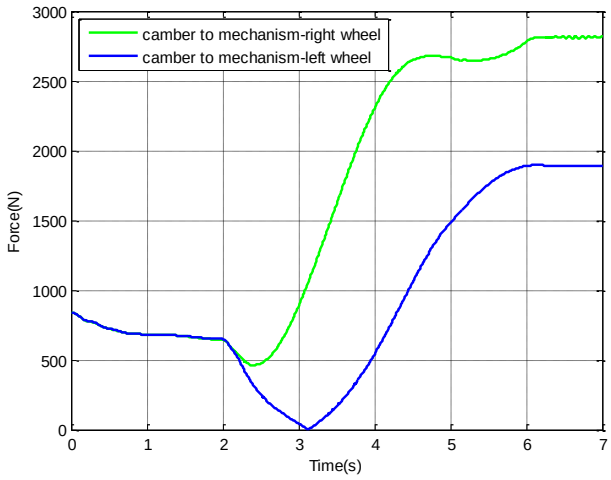

Figure 4-27. Force vs. time for joints attaching camber links to mechanisms when the vehicle is turning, accelerating, and cambering, at the same time.

Figure 4-28 demonstrates the vertical tire force distribution among all three wheels when the vehicle is turning, accelerating, and at the same time camber is applied to the wheels. It can be seen in this diagram that until the 6th s, since a positive acceleration is applied to the vehicle, larger forces are transferred to the rear wheel, in comparison to the front wheels. After the 2nd s, lateral load transfer takes place, which causes an imbalance between the forces developed at the front wheels. Hence, because of turning to the right, more loads are applied to the left wheel and consequently, more vertical forces on the left side have been sensed.

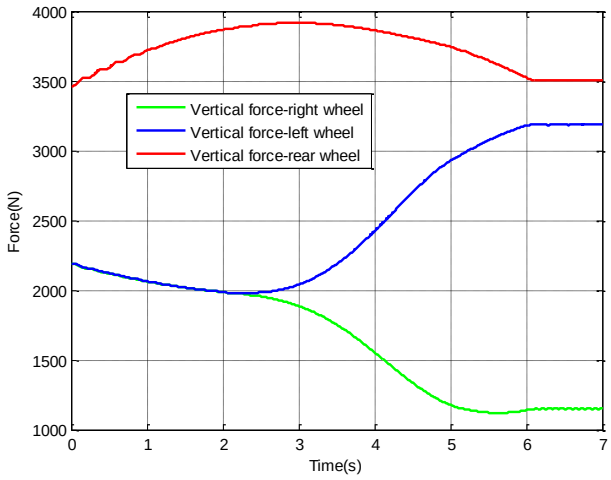

Figure 4-28. Vertical tire forces on all three wheels when the vehicle is turning, accelerating, and cambering, at the same time.

In this chapter, ride quality of the three-wheeled vehicle was analyzed, first, by using an analytical method and then a commercial computer program. The analytical method was done by developing a 6-DOF model. Doing so, first the transfer functions for the transmissibility of road irregularities to the body were calculated. Using these functions and by plotting the corresponding bode diagrams, it was determined that the rear wheel transfers larger magnitudes of road irregularities to the body. Besides, it was found out that at high frequencies, a lighter unsprung mass is required to develop smaller transmissibility ratios, while at low frequencies, it was shown that this parameter is not sensitive to the unsprung mass. In addition, for the ride comfort analysis, vertical displacement, vertical acceleration, and pitch angle of the vehicle when the car was going over different types of roads were also discussed. Two main road irregularities (a single bump and a sinusoidal road profile) were used as the input to the model.

In the next step, Multibody Dynamics Adams software was used to calculate forces in the joints of the suspension system. By assuming constant lateral, vertical, and longitudinal accelerations, the developed forces were calculated (static analysis). In the second approach, the same analysis was carried out but for cases where the vehicle moved at various speeds over various roads (dynamic analysis). The forces calculated in the dynamic analysis were smaller than those measured in the static analysis, as expected, given that the static analysis was carried out with applying very large input accelerations to determine a safe margin for the performance of the vehicle suspension system.

The behaviour of the suspension system was also studied over a particular road (single haversine bump) with two different methods (analytical and simulation), in order to verify the accuracy of both methods. Comparison between the results obtained from these two methods showed the ability of both methods to determine the forces at various parts of the suspension system. The MATLAB code for ride comfort analysis can be found in Appendix B.

Chapter 5. Concluding Remarks and Recommendations

This thesis evaluated the lateral dynamics, roll stability, handling, and ride dynamics of a three-wheeled vehicle with tadpole design. The primary objective was to study the effects of adding active camber system on the vehicle dynamic performance. In addition to evaluating the performance of the suspension in regards to the ride quality of the vehicle, load case studies were also performed to evaluate both the static and dynamic forces on the suspension parts under different operating scenarios. The major highlights of this dissertation are summarized below:

- A 3-DOF model was formulated to analyze the handling characteristics and related transfer functions were derived.
- The handling characteristics of the vehicle were studied by determining the effects of camber angle on yaw rate, via using the derived transfer functions and plotting the corresponding bode diagrams.
- The lateral/roll stability of the vehicle was evaluated in terms of skid and rollover threshold, which were assessed by estimating the lateral acceleration threshold of the vehicle during severe cornering maneuver.
- A 6-DOF ride dynamic model of the vehicle was also formulated to investigate the ride dynamic performance of the vehicle under two different road inputs through simulations in MATLAB software. The ride dynamic performance of the vehicle was evaluated in terms of vertical displacement, vertical acceleration, and pitch angle of the sprung mass. To study the transmissibility of road irregularities to the body, the corresponding transfer functions were derived and their bode diagrams were plotted and analyzed.
- A multi-body dynamic model of the vehicle wheel assembly, including the suspension, was developed in Adams software in order to evaluate both the static and dynamic forces on the suspension parts under different steering and road inputs.

5.1 Conclusions

The main conclusions of this work are summarized below:

- The effect of camber angle on yaw rate becomes more elaborate (at low frequencies) when the vehicle longitudinal speed of the vehicle increases.
- The static stability factor (i.e., lateral acceleration threshold) of the vehicle was improved by applying negative camber angles to the outside-turn wheel, regardless of the direction of the camber angle on the inside-turn wheel.

- Both the vehicle rollover and skid could happen at different camber angles and on different roads. The results concluded that upon driving on wet, snowy, and icy roads, it is more possible that skidding takes place, while the rollover tendency of the vehicle is higher on dry roads.

- The ride dynamic analysis of the vehicle clearly illustrated that the three-wheeled vehicle showed a reasonable ride performance. However, the transmissibility of the road to the body in different frequencies could be reduced by decreasing the unsprung mass.

- The suspension loading analyses showed that the rear wheel suspension tolerated larger forces in comparison to those at the front during the acceleration time, which is mainly attributed to tadpole geometry and longitudinal load transfers from the front to the back of the vehicle during acceleration

- The obtained results illustrated that even the largest dynamic forces developed during the movement of the vehicle in various roads and in different conditions (e.g., turning, cambering, accelerating, etc.) were still smaller than those measured in the static analysis, which verified the existence of a safe margin for the performance of the vehicle suspension system.

5.2 Recommendations

Several studies that can be carried out in the future to improve the accuracy and coherency of this work are:

- A more refined nonlinear model of the vehicle can be used to improve the results.

- The rollover index could be also considered as a desired assessment to evaluate the vehicle roll stability.
- In order to improve the vehicle lateral/roll stability, stability control systems such as yaw rate/side slip angle-based controller could be developed.
- A skid prevention system can be also designed for this vehicle based on the measurement of the side slip angle and wheel slip.
- A complete FEA analysis could be performed on the suspension parts based on the static and dynamic forces obtained in this study.

Appendix A. MATLAB code for handling analysis and lateral acceleration threshold

Lateral acceleration threshold study

```
clc
clear all
close all
g=9.8;% m/(s^2)
m=900;% (KG)vehicle mass
h=.2;%(m)cg to roll centre
H=.5;%(m)cg to ground
N=0;
phi=0; %roll angle
r=.28; %(m)tire radius
a=.8; %(m)front to cg distance
b=1; %(m) rear to cg distance
l=a+b; %total lenght
rr=20;
g1=rr*(pi/180);%camber 1
g2=rr*(pi/180); %camber 2
g3=rr*(-pi/180);%camber 3
ax=0;


T=1.4; %(m)track
M=(l*r*sin(g3))/((T/2)+(r*(sin(g1)-sin(g3))));


teta1=atan(((T/2)+r*sin(g1))/(l+M));
num1=((T+2*r*sin(g1))*b*g*cos(teta1))-(2*(l+M)*h*sin(phi)*g);
d1=h*(1-cos(phi));
d2=(((1-cos(g1))+(1-cos(g2)))*(r*b/l)*(1/2))+(r*(1-cos(g3)));

denom1=(H-d1-d2)*2*(l+M)*cos(teta1);
ay=(num1/denom1)+((ax*sin(teta1))/cos(teta1));
kt=20000;
phi=(m*ay*h)/(kt-(m*g*h))

teta1=atan(((T/2)+r*sin(g1))/(l+M));
num1=((T+2*r*sin(g1))*b*g*cos(teta1))-(2*(l+M)*h*sin(phi)*g);
d1=h*(1-cos(phi));
d2=((1-cos(g1))+(1-cos(g2))+(1-cos(g3)))*r*(1/3);

denom1=(H-d1-d2)*2*(l+M)*cos(teta1);
ay1=(num1/denom1)+((ax*sin(teta1))/cos(teta1));
ay=ay/g
ay1=ay1/g
RolG=(phi/ay);
```

Handling analysis study

```
clc
clear all
close all
 ca1=25000;
 ca2=25000;
 ca3=40000;
 M=900;
 u=50/3.6;
 a=.8;
```

```
 T=1.4;
 ks=12000;
 cs=800;
 b=1;
 ms=780;
 Ix=210;
 hh=0.3;
 ct=0.2*cs*T^2;
 kt=0.2*ks*T^2;
 h=0.5;
 g=9.8;
 cg1=0.1*ca1;
 cg2=0.1*ca2;
 cg3=0.1*ca3;
 Iz=81;
 Tf=20;

 %%%%%%%%%%%Input
gg1=0/57.22;
gg2=0;
gg3=0/57.22;
d1=0;
d2=0;
d3=0;

%%%%%%%%%%%% MATRIX A
a11=(-ca1-ca2-ca3)/(M*u);
a12=(((-a*ca1)+(b*ca2)-(a*ca3))/(M*u))-u;
a13=0;
a14=0;
a15=0;

a21=(-a*ca1-a*ca3+b*ca2)/(Iz*u);
a22=(-((a)^2)*ca1-((a)^2)*ca3-((b)^2)*ca2)/(Iz*u);
a23=0;
a24=0;
a25=0;

a31=0;
a32=-(ms/Ix)*hh*u;
a33=-(ct/Ix);
a34=-(kt-ms*g*h)/Ix;
a35=-(ms*hh)/Ix;

a41=0;a42=0;a43=1;a44=0;a45=0;
a51=0;a52=0;a53=0;a54=0;a55=0;


A=[a11 a12 a13 a14 a15;
   a21 a22 a23 a24 a25;
   a31 a32 a33 a34 a35;
   a41 a42 a43 a44 a45;
   a51 a52 a53 a54 a55];

%%%%%%%%%%%%%%%%%%% MATRIX B
b11=0;
b12=cg1/M;
b13=cg2/M;
b14=cg3/M;
b15=ca1/M;
b16=ca2/M;
b17=ca3/M;

b21=1/Iz;
b22=a*cg1/Iz;
b23=-b*cg2/Iz;
b24=a*cg3/Iz;
```

```
b25=a*ca1/Iz;
b26=-b*ca2/Iz;
b27=a*ca3/Iz;

b31=0;b32=0;b33=0;b34=0;b35=0;b36=0;b37=0;
b41=0;b42=0;b43=0;b44=0;b45=0;b46=0;b47=0;
b51=0;b52=0;b53=0;b54=0;b55=0;b56=0;b57=0;

B=[b11 b12 b13 b14 b15 b16 b17;
   b21 b22 b23 b24 b25 b26 b27;
   b31 b32 b33 b34 b35 b36 b37;
   b41 b42 b43 b44 b45 b46 b47;
   b51 b52 b53 b54 b55 b56 b57];
%%%%%%%%%%%%%%%%%%%%%%%%%%%%%%%%%%%%%%%%%%%%%%%%%%%%
CC = {'k','b','r','g','y',[.5 .6 .7],[.8 .2 .6]}; % Cell array of colros.
for j=1:4;
C = eye(5);
D= zeros(5,7);
Tstep=0.001;
T = 0:Tstep:Tf;
Mzdyc=0*ones(size(T));
g1=gg1(j).*ones(size(T));
g2=gg2(j).*ones(size(T));
g3=gg3(j).*ones(size(T));
d1=d1.*ones(size(T));
d2=d2.*ones(size(T));
d3=d3.*ones(size(T));
U=[Mzdyc;g1;g2;g3;d1;d2;d3];
sys=ss(A,B,C,D);
[y,t]=lsim(sys, U, T);
r=y(:,2);
v=y(:,1);
phi=y(:,4);

for i=Tstep:Tstep:Tf

    TT=Tstep:Tstep:i+Tstep;
    p=r(1:(round((i+Tstep)/Tstep)));
    sai((round((i+Tstep)/Tstep)),1)= trapz(TT,p);

    hold on
end


Xdot=u.*cos(sai)-v.*sin(sai);
Ydot=u.*sin(sai)+v.*cos(sai);

for i=Tstep:Tstep:Tf

    TT=Tstep:Tstep:i+Tstep;
    q=Xdot(1:(round((i+Tstep)/Tstep)));
    X((round((i+Tstep)/Tstep)),1)= trapz(TT,q);

%     hold on
end

for i=Tstep:Tstep:Tf

    TT=Tstep:Tstep:i+Tstep;
    g=Ydot(1:(round((i+Tstep)/Tstep)));
    Y((round((i+Tstep)/Tstep)),1)= trapz(TT,g);

%     hold on
end
```

Appendix B. MATLAB code for ride analysis

```
clc
clear all
close all

Csfl=1200;
Csfr=1200;
Csr=2000;
T=1.4; %meter
T2=T/2;
a=.8; %meter
b=1; %meter
l=a+b; %meter
ms=750;
Ksfl=6000;
Ksfr=6000;
Ksr=8000;
Ix=210;
mufl=50;%kg
mufr=50;%kg
mur=50;%kg
Ktr=230000;
Ktfl=230000;
Ktfr=230000;
Iy=480;
Tf=10;%second
d=.1;
lamda=1;
v=20/3.6;
Tstep=0.001;

T = 0:Tstep:Tf;   % simulation time = 10 seconds

yfr=d*(1/2)*(1-cos((2*pi*v/(lamda))*(T-l/v))); %road input
yfl=d*(1/2)*(1-cos((2*pi*v/(lamda))*(T-l/v))); %road input
yr=d*(1/2)*(1-cos((2*pi*v/(lamda))*T));


yfr(((((lamda/v))/Tstep)):end)=0;
yfl((((lamda/v)/Tstep)):end)=0;
yr(((lamda/(v))/Tstep):end)=0;


%%%%%%%%%%%%%%%%%%%%%%%%%MATRIX A
a11=(-Csfl-Csfr-Csr)/ms;
a12=((-T2*Csfl)+(T2*Csfr))/ms;
a13=((a*Csfl)+(a*Csfr)-(b*Csr))/ms;
a14=Csfl/ms;
a15=Csfr/ms;
a16=Csr/ms;
a17=(-Ksfl-Ksfr-Ksr)/ms;
a18=((-T2*Ksfl)+(T2*Ksfr))/ms;
a19=((a*Ksfl)+(a*Ksfr)-(b*Ksr))/ms;
a110=Ksfl/ms;
a111=Ksfr/ms;
a112=Ksr/ms;

a21=((-Csfl*T2)+(Csfr*T2))/Ix;
a22=((-Csfl*(T2^2))+(Csfr*(T2^2)))/Ix;
a23=((Csfl*T2*a)-(Csfr*T2*a))/Ix;
a24=Csfl*T2/Ix;
a25=(-Csfr*T2)/Ix;
a26=0;
a27=((-Ksfl*T2)+(Ksfr*T2))/Ix;
```

```
a28=((-Ksfl*(T2^2))+(Ksfr*(T2^2)))/Ix;
a29=((Ksfl*T2*a)-(Ksfr*T2*a))/Ix;
a210=Ksfl*T2/Ix;
a211=-Ksfr*T2/Ix;
a212=0;

a31=((Csfl*a)-(Csr*b)+(Csfr*a))/Iy;
a32=((Csfl*a*T2)-(Csfr*a*T2))/Iy;
a33=((-Csfl*(a^2))-(Csr*(b^2))-(Csfr*(a^2)))/Iy;
a34=(-Csfl*a)/Iy;
a35=-Csfr*a/Iy;
a36=Csr*b/Iy;
a37=(Ksfl*a-Ksr*b+Ksfr*a)/Iy;
a38=(Ksfl*a*T2-Ksfr*a*T2)/Iy;
a39=((-Ksfl*(a^2))-(Ksr*(b^2))-Ksfr*(a^2))/Iy;
a310=-Ksfl*a/Iy;
a311=-Ksfr*a/Iy;
a312=Ksr*b/Iy;

a41=Csfl/mufl;
a42=Csfl*T2/mufl;
a43=-Csfl*a/mufl;
a44=-Csfl/mufl;
a45=0;
a46=0;
a47=Ksfl/mufl;
a48=Ksfl*T2/mufl;
a49=-Ksfl*a/mufl;
a410=(-Ksfl-Ktfl)/mufl;
a411=0;
a412=0;

a51=Csfr/mufr;
a52=-Csfr*T2/mufr;
a53=-Csfr*a/mufr;
a54=0;
a55=-Csfr/mufr;
a56=0;
a57=Ksfr/mufr;
a58=-Ksfr*T2/mufr;
a59=-Ksfr*a/mufr;
a510=0;
a511=(-Ksfr-Ktfr)/mufr;
a512=0;

a61=Csr/mur;
a62=0;
a63=Csr*b/mur;
a64=0;
a65=0;
a66=-Csr/mur;
a67=Ksr/mur;
a68=0;
a69=Ksr*b/mur;
a610=0;
a611=0;
a612=(-Ksr-Ktr)/mur;

a71=1;a72=0;a73=0;a74=0;a75=0;a76=0;a77=0;a78=0;a79=0;a710=0;a711=0;a712=0;

a81=0;a82=1;a83=0;a84=0;a85=0;a86=0;a87=0;a88=0;a89=0;a810=0;a811=0;a812=0;

a91=0;a92=0;a93=1;a94=0;a95=0;a96=0;a97=0;a98=0;a99=0;a910=0;a911=0;a912=0;

a101=0;a102=0;a103=0;a104=1;a105=0;a106=0;a107=0;a108=0;a109=0;a1010=0;a1011=0;a1012=0;
```

```
aa111=0;aa112=0;aa113=0;aa114=0;aa115=1;aa116=0;aa117=0;aa118=0;aa119=0;aa1110=0;aa1111=0;aa1
112=0;

aa121=0;aa122=0;aa123=0;aa124=0;aa125=0;aa126=1;aa127=0;aa128=0;aa129=0;aa1210=0;aa1211=0;aa1
212=0;

A=[a11 a12 a13 a14 a15 a16 a17 a18 a19 a110 a111 a112;
   a21 a22 a23 a24 a25 a26 a27 a28 a29 a210 a211 a212;
   a31 a32 a33 a34 a35 a36 a37 a38 a39 a310 a311 a312;
   a41 a42 a43 a44 a45 a46 a47 a48 a49 a410 a411 a412;
   a51 a52 a53 a54 a55 a56 a57 a58 a59 a510 a511 a512;
   a61 a62 a63 a64 a65 a66 a67 a68 a69 a610 a611 a612;
   a71 a72 a73 a74 a75 a76 a77 a78 a79 a710 a711 a712;
   a81 a82 a83 a84 a85 a86 a87 a88 a89 a810 a811 a812;
   a91 a92 a93 a94 a95 a96 a97 a98 a99 a910 a911 a912;
   a101 a102 a103 a104 a105 a106 a107 a108 a109 a1010 a1011 a1012;
   aa111 aa112 aa113 aa114 aa115 aa116 aa117 aa118 aa119 aa1110 aa1111 aa1112;
   aa121 aa122 aa123 aa124 aa125 aa126 aa127 aa128 aa129 aa1210 aa1211 aa1212];


%%%%%%%%%%%%%%%%%%%%%%%%%%MATRIX B

b11=0;b12=0;b13=0;
b21=0;b22=0;b23=0;
b31=0;b32=0;b33=0;
b41=Ktfl/mufl;b42=0;b43=0;
b51=0;b52=Ktfr/mufr;b53=0;
b61=0;b62=0;b63=Ktr/mur;
b71=0;b72=0;b73=0;
b81=0;b82=0;b83=0;
b91=0;b92=0;b93=0;
b101=0;b102=0;b103=0;
b111=0;b112=0;b113=0;
b121=0;b122=0;b123=0;

B=[b11 ,b12, b13;
    b21 ,b22, b23;
    b31 ,b32, b33;
    b41 ,b42, b43;
    b51 ,b52, b53;
    b61 ,b62, b63;
    b71 ,b72, b73;
    b81 ,b82, b83;
    b91 ,b92, b93;
    b102 ,b102, b103;
    b111 ,b112, b113;
    b121 ,b122, b123];


%%%%%%%%%%%%%%%%%%%%%%%%%%%%%%%%%%%%%%%%%%%%%%%%%%%%%%%%%%%%%%%%
C = eye(12);
D= zeros(12,3);
Tstep=0.01;               % simulation time = 10 seconds
U=[yfl;yfr;yr];% no input
sys=ss(A,B,C,D);
[y,t]=lsim(sys, U, T);
```

Bibliography

[1] J. Y. Wong, *Theory of Ground Vehicles*, 3rd Edition, John Wiley and Sons, Inc, 2001.

[2] K. -P. Kruger, A. Neukum, J. Schuller, *A Workload Approach to the Evaluation of Vehicle Handling Characteristics*, SAE Technical Paper Series, SAE 2000 World Congress, Detroit, USA, 2000.

[3] T. D. Gillespie, *Fundamentals of Vehicle Dynamics*, Society of Automotive Engineers, 1992.

[4] L. D. Metz, *What Constitutes Good Handling*, SAE Technical Paper, 2004-01-3532, 2004.

[5] R. Rajamani, *Vehicle Dynamics and Control*, 2nd Edition, Springer, 2006.

[6] P. S. Els, N. J. Theron, P. E. Uys, M. J. Thoresson, *The Ride Comfort vs. Handling Compromise for Off-Road Vehicles*, Journal of Terramechanics, 44, 303-317, 2007.

[7] P. Barak, *Magic Numbers in Design of Suspensions for Passengers Cars*, SAE Technical Paper, 911921, 1991.

[8] W. Bergman and D. Pelargus, *The Role of Steer and Sideslip in the Mechanism of Slip Angle*, SAE Technical Paper, 960999, 1996.

[9] G. -D. Yin, N. Chen, J. -X. Wang, L. -Y. Wu, *A Study on μ-Synthesis Control for Four-Wheel Steering System to Enhance Vehicle Lateral Stability*, Journal of Dynamic Systems, Measurement, and Control, 133, 011002-1, 2011.

[10] L. Segel, *On the Lateral Stability and Control of the Automobile as Influenced by Dynamics of the Steering System*, Journal of Engineering for Industry, 88, 283-294,1966.

[11] G. -D. Yin, *Estimating Lateral Stability Region for Four Wheel Independently – Actuated Electric Vehicle Considering Steering*, SAE Technical Paper, 2013-01-2373, 2013.

[12] J. Samsundar and J. C. Huston, *Estimating Lateral Stability Region of a Nonlinear 2 Degree-of-Freedom Vehicle*, SAE Technical Paper, 981172, 1998.

[13] H. Lv and Sh. Liu, *Closed-Loop Handling Stability of 4WS Vehicle with Yaw Rate Control*, Journal of Mechanical Engineering, 59, 595-603, 2013.

[14] A. Hac and M. D. Simpson, *Estimation of Vehicle Side Slip Angle and Yaw rate*, SAE Technical Paper, 2000-01-0696, 2000.

[15] Y. Feng, Z. Yu, L. Xiong, J. Liu, C. Jin, *Torque Vectoring Control for Distributed Drive Electric Vehicle Based on State Variable Feedback*, SAE International Journal of Passenger Cars- Electronic and Electrical Systems, 7, 328-336, 2014.

[16] M. Hiemer, S. Lehr, U. Kiencke, T. Matsunaga, *A Fuzzy System to Determine the Vehicle Yaw Angle*, SAE Technical Paper, 2004-01-1191, 2004.

[17] F. Lin and Y. Zhao, *A Comparison of Two Soft-Sensing Methods for Estimating Vehicle Side Slip Angle*, SAE Technical Paper, 2007-01-3587, 2007.

[18] S. Williams and A. Nhila, *Handling Comparison of Vehicles with Steerable Auxiliary Axles*, SAE International Journal of Commercial Vehicles, 6, 281-287, 2013.

[19] N. Matsumoto and M. Tomizuka, *Vehicle Lateral Velocity and Yaw Rate Control with Two Independent Control Inputs*, IEEE American Control Conference, San Diego, California, 1990.

[20] Y. Zeyada, D. Karnopp, M. El-Arabi, E. El-Behiry, *A Combined Active-Steering Differential-Braking Yaw rate Control Strategy for Emergency Maneuvers*, SAE Technical Paper, 980230, 1998.

[21] E. Sabbioni, F. Cheli, M. Vignati, S. Melzi, *Comparison of Torque Vectoring Control Strategies for a IWM Vehicle*, SAE International Journal of Passenger Cars- Electronic and Electrical Systems, 7, 565-572, 2014.

[22] S. Sakhalkar, P. Dhillon, P. Kumar, S. Bakshi, P. S. Arora, *Implementation of an Electronic Differential Using Torque Vectoring*, SAE Technical Paper, 2014-01-1776, 2014.

[23] M. A. Zakaria, H. Zamzuri, R. Mamat, S. A. Mazlan, *A Path Tracking Algorithm Using Future Prediction Control with Spike Detection for an Autonomous Vehicle Robot*, International Journal of Advanced Robotic System, 10, 309, 2013.

[24] C. G. Liang, *A Constant Radius Constant Speed Simulation Methodology-Yaw Rate Control*, SAE Technical Paper, 2011-01-0738, 2011.

[25] G. Baffet, A. Charara, J. Stephant, *Sideslip Angle, Lateral Tire Force and Road Friction Estimation in Simulations and Experiments*, IEEE International Conference on Control Applications, Munich, Germany, 2006.

[26] H. Sasaki and T. Nishimaki, *A Side-Slip Angle Estimation Using Neural Network for a Wheeled Vehicle*, SAE Technical Paper, 2000-01-0695, 2000.

[27] Retrieved from http://www.hunter.com/alignment/hd/995T-2.pdf on October 12, 2014

[28] S. -J. Park and J. -H. Sohn, *Effects of Camber Angle Control of Front Suspension on Vehicle Dynamic Behaviours*, Journal of Mechanical Science and Technology, 26, 307-313, 2011.

[29] T. Yoshino and H. Nozaki, *Camber Angle Control Method Corresponding to the Electric Vehicle Age*, Scientific Research, 6, 472-484, 2014.

[30] A. Woodruff, B. Surgenor, C. Knobel, *Comparison of Methods to Improve Camber Using a Modelica/Dymola Multi-Body Model*, SAE Technical Paper, 2007-01-0837, 2007.

[31] Y. Yoshini and H. Nozaki, *About the Effect of Camber Control on Vehicle Dynamics*, SAE Technical Paper, 2014-01-2383, 2014.

[32] J. F. Cuttino, J. S. Shepherd, M. N. Sinha, *Design and Development of an Optimized, Passive Camber System for Vehicles*, SAE Technical Paper, 2008-01-2950, 2008.

[33] R. Vieira, L. Nicolazzi, N. Roqueiro, R. Padilha, *Modeling and analysis of dynamic behavior of tilting vehicle*, SAE Technical Paper, 2007-01-2869, 2007.

[34] S. Kim, J. McPhee, N. L. Azad, *Improving Stability of a Narrow Track Personal Vehicle using an Active Tilting System*, SAE Technical Paper, 2014-01-0087, 2014.

[35] J. Berote, A. Van Poelgeest, J. Darling, K. Edge, A. Plummer, *The Dynamics of a Three-Wheeled Narrow-Track Tilting Vehicle*, FISITA World Automotive Congress, Munich, Germany 2008.

[36] J. Edelmam and M. Plochl, *Electronic Stability Control of a Narrow Tilting Vehicle*, SAE International Journal of Materials and Manufacturing, 4, 1006-1013, 2011.

[37] F. Will, J. N. Davidson, P. Couchman, D. Bednall, *Tomorrow's Car-for Today's People: Can Tilting Three Wheeled Vehicle be a Solution for the Problems of Today and the Future?*, SAE Technical Paper, 2011-28-0001, 2011.

[38] N. A. El-Esnawy and J. F. Wilson, *Lateral Dynamics and Stability of Two Vehicles in Tandem*, Journal of Dynamics, Measurement, and Control, 120, 51-56, 1998.

[39] G. Erdogan, F. Borrelli, R. Tebano, G. Audisio, G. Lori, J. Sannazzaro, *Development of a New Lateral Stability Control System Enhanced with Accelerometer Based Tire Sensors*, ASME Dynamic System and Control Conference, Cambridge, USA, 2010.

[40] W. A. Oraby, *Improvement of Vehicle Lateral Stability during Overtaking Process by Active Front Steering System*, SAE Technical Paper, 2007-01-0810, 2007.

[41] W. A. Oraby, M. A. Aly, S. M. El-Demerdash, A. M. Selim, *Interaction of Vehicle Ride Vibration Control with Lateral Stability Using Active Rear Wheel Steering*, SAE Technical Paper, 2009-01-1042, 2009.

[42] J. Yoon, Wanki Cho, K. Yi, *Vehicle Stability Control Scheme for Rollover Prevention and Maneuverabiliyu/Lateral Stability Improvement*, SAE Technical Paper, 2009-01-0826, 2009.

[43] B. C. Jang and R. P Marimuthu, *Sensitivity Analysis of SUV Parameters on Rollover Propensity*, International Journal of Automotive Technology, 7, 703-714, 2006.

[44] B. Johansson and M Gafvert, *Untripped SUV Rollover Detection and Prevention*, 43rd IEEE Conference on Decision and Control, Atlantis, Bahamas, 2004.

[45] D. Odenthal, T. Bunte, J. Ackermann, *Nonlinear steering and Braking Control for Vehicle Rollover Avoidance*, European Control Conference, Karlsruhe, Germany,1999.

[46] K. Bedsworth, R. Butler, G. Rogers, K. Breen, W. Fischer, *Commercial Vehicle skid Distance Testing and Analysis*, SAE Technical Paper, 2013-01-0771, 2013.

[47] W. Bartlett, R. Baxter, E. Livesay, B. Schmidt, T. Stanard, W. Wright, *Comparison of Drag-Sled and Skidding-Vehicle Drag Factors on Dry Roadways*, SAE Technical Paper, 2006-01-1398, 2006.

[48] G. Previati, M. Gobbi, G. Mastinu, *Friction Coefficient on Snowy and Icy Surfaces of Pneumatic Tires Fitted with or without Anti-Skid Devices*, SAE Technical Paper, 2006-01-0560, 2006.

[49] K. M. Marshek and J. F. Cuderman, *Performance of Anti-Lock Braking System Equipped Passenger Vehicles-Part II: Braking as a Function of Initial Vehicle Speed in Braking Maneuver*, SAE Technical Paper, 2002-01-0307, 2002.

[50] W. Bartlett and W. Wright, *Braking on Dry Pavement and Gravel With and Without ABS*, SAE Technical Paper, 2010-01-0066, 2010.

[51] S. Hess, *Automobile Riding-Comfort*, SAE Technical Paper, 240038, 1924.

[52] A. Deb and D. Joshi, *A study on Ride Comfort Assessment of Multiple Occupants using Lumped Parameter Analysis*, SAE Technical Paper, 2012-01-0053, 2012.

[53] M. K. Naidu, S. S. Rao, T. Tejesh, *Ride Analysis of Three Wheeled Vehicle Using MATLAB/Simulink*, AMAE International Journal on Manufacturing and Material Science, 2, 22-26, 2012.

[54] B. S. Kim, K. J. Joo, K. I. Bae, *Ride Comfort Improvement of a Compact SUV Considering Driving Maneuver and Road Surface*, SAE Technical Paper, 2011-01-0558, 2011.

[55] K. Ogata, *Modern Control Engineering*, 5th Edition, Prentice Hall, 2011.

[56] J. Ackermann, *Robust Control Prevents Car Skidding*, Control Systems, IEEE, 17, 23-31, 1997.

[57] T. Sun, Y. Zhang, P. Barak, *4-DOF Vehicle Ride Model*, SAE Technical Paper, 2002-01-1580, 2002.

[58] P. Kumbhar, P. Xu, J. Yang, *Evaluation of Human Body Response for Different Vehicle Seats Using a Multibody Biodynamic Model*, SAE Technical Paper, 2013-01-0994, 2013.

[59] G. Fichera, M. Scionti, F. Garesci, *Experimental Correlation between the Road Roughness and the Comfort Perceived in Bus Cabins*, SAE Technical Paper, 2007-01-0352, 2007.

[60] A. M. A. Soliman, S. M. Moustafa, A. O. M. Shogae, *Parameters Affecting Vehicle Ride Comfort Using Half Vehicle Model*, SAE Technical Paper, 2008-01-1146, 2008.

[61] K. EI Majdoub, D. Ghani, F. Giri, F. Z. Chaoui, *Adaptive Semi-Active Suspension of Quarter-Vehicle with Magnetorheological Damper*, Journal of Dynamic Systems, Measurement, and Control, 137, 021010, 2014.

[62] M. Blundell and D. Harty, *Multibody Systems Approach to Vehicle Dynamics*, SAE, Elsevier Butterworth-Heinemann publications, 2004.

[63] V. V. Solanki and N. S. Patel, *Rigid Body and Modal Analysis of Independent Suspension Link*, International Journal of Thesis Project and Dissertations (IJTPD), 2, 35-46, 2014.

[64] M. J. Stallmann and P.S. Els, *Parameterization and Modelling of Large Off-Road Tyres for Ride Analyses: Part 2- Parameterization and Validation of Tyre Models*, Journal of Terramechanics, 55, 85-94, 2014.